

# Northumbria Research Link

Citation: Woodward, John, Hein, Andrew S., Winter, Kate, Westoby, Matt, Marrero, Shasta M., Dunning, Stuart A., Lim, Michael, Rivera, Andrés and Sugden, David E. (2022) Blue-ice moraines formation in the Heritage Range, West Antarctica: Implications for ice sheet history and climate reconstruction. *Quaternary Science Advances*, 6. p. 100051. ISSN 2666-0334

Published by: Elsevier

URL: <https://doi.org/10.1016/j.qsa.2022.100051>  
<<https://doi.org/10.1016/j.qsa.2022.100051>>

This version was downloaded from Northumbria Research Link:  
<http://nrl.northumbria.ac.uk/id/eprint/48748/>

Northumbria University has developed Northumbria Research Link (NRL) to enable users to access the University's research output. Copyright © and moral rights for items on NRL are retained by the individual author(s) and/or other copyright owners. Single copies of full items can be reproduced, displayed or performed, and given to third parties in any format or medium for personal research or study, educational, or not-for-profit purposes without prior permission or charge, provided the authors, title and full bibliographic details are given, as well as a hyperlink and/or URL to the original metadata page. The content must not be changed in any way. Full items must not be sold commercially in any format or medium without formal permission of the copyright holder. The full policy is available online: <http://nrl.northumbria.ac.uk/policies.html>

This document may differ from the final, published version of the research and has been made available online in accordance with publisher policies. To read and/or cite from the published version of the research, please visit the publisher's website (a subscription may be required.)



## Blue-ice moraines formation in the Heritage Range, West Antarctica: Implications for ice sheet history and climate reconstruction

John Woodward<sup>a,\*</sup>, Andrew S. Hein<sup>b</sup>, Kate Winter<sup>a</sup>, Matthew J. Westoby<sup>a</sup>, Shasta M. Marrero<sup>b,c</sup>, Stuart A. Dunning<sup>d</sup>, Michael Lim<sup>e</sup>, Andrés Rivera<sup>f</sup>, David E. Sugden<sup>b</sup>

<sup>a</sup> Department of Geography and Environmental Sciences, Engineering and Environment, Northumbria University, Newcastle Upon Tyne, UK

<sup>b</sup> School of GeoSciences, University of Edinburgh, Edinburgh, UK

<sup>c</sup> School of Earth and Ocean Sciences, Cardiff University, Cardiff, UK

<sup>d</sup> School of Geography, Politics and Sociology, Newcastle University, Newcastle Upon Tyne, UK

<sup>e</sup> Department of Mechanical and Construction Engineering, Engineering and Environment, Northumbria University, Newcastle Upon Tyne, UK

<sup>f</sup> Departamento de Geografía, Universidad de Chile, Santiago, Chile

### ARTICLE INFO

#### Keywords:

Blue ice moraine  
Geophysical surveys  
Cosmogenic nuclide dating  
West Antarctic ice sheet  
Ice sheet history

### ABSTRACT

Blue ice is found in areas of Antarctica where katabatic winds, focussed by steep surface slopes or by topography around nunataks, cause enhanced surface ablation. This process draws up deeper, older ice to the ice sheet surface, often bringing with it englacial sediment. Prevailing theories for dynamically stable moraine surfaces in East Antarctica suggest that: (i) it is this material, once concentrated, that forms blue-ice moraines (BIM), (ii) that the moraine formation can be dated using cosmogenic isotope approaches, and that, (iii) since we expect an increase in exposure age moving away from the ice margin towards bedrock, dating across the moraine can be used to constrain ice-sheet history. To test this lateral accretion model for BIM formation we visited Patriot, Marble and Independence Hills in the southern Heritage Range, West Antarctica. Detailed field surveys of surface form, sediment and moraine dynamics were combined with geophysical surveys of the englacial structure of the moraines and cosmogenic nuclide analysis of surface clasts. Results suggest sediment is supplied mainly by basal entrainment, supplemented by debris-covered valley glaciers transferring material onto the ice sheet surface, direct deposition from rock-fall and slope processes from nunataks. We find that once sediment coalesces in BIM, significant reworking occurs through differential ablation, slope and periglacial processes. We bring these processes together in a conceptual model, concluding that many BIM in West Antarctica are dynamic and, whilst they persist through glacial cycles, they do not always neatly record ice sheet retreat patterns since linear distance from the ice margin does not always relate to increased clast exposure age. Understanding the dynamic processes involved in moraine formation is critical to the effective interpretation of the typically large scatter of cosmogenic nuclide exposure ages, opening a deep window into the million-year history of the West Antarctic Ice Sheet.

### 1. Introduction

Blue-ice areas (BIA) were first described scientifically in Antarctica by Schytt (1961). Commonly they form in areas where katabatic winds are enhanced by steeper surface slopes, topography or the presence of nunataks (Takahashi et al., 1992). They represent areas of surface mass loss of ice due mainly to sublimation, especially in summer (Bintanja, 1999). In compensation for the loss of surface ice there is upward compressive flow of ice which may bring debris to the surface concentrating, for example, rocks derived from erosion of the glacier bed,

entrainment of basal debris or meteorites falling onto the inner reaches of the ice sheet (Whillans and Cassidy, 1983; Altmaier et al., 2010). The age of the ice in BIA ranges from 10 to 100 ka in Dronning Maud Land (Sinisalo et al., 2007) and the Ellsworth Mountains (Turney et al., 2013; Turney et al., 2020) to ages of 100–600 ka in the Allan Hills (Spaulding et al., 2013; Whillans and Cassidy, 1983) and adjacent to Mount Achernar (Kaplan et al., 2017), and over 2 million years in Ong Valley (Bibby et al., 2016), the latter two sites lying in the Transantarctic Mountains. One meteorite in the Allan Hills had an exposure age of 2.2 million years (Scherer et al., 1997). Ages of debris associated with BIA in

\* Corresponding author.

E-mail address: [john.woodward@northumbria.ac.uk](mailto:john.woodward@northumbria.ac.uk) (J. Woodward).

<https://doi.org/10.1016/j.qsa.2022.100051>

Received 25 August 2021; Received in revised form 6 January 2022; Accepted 17 January 2022

Available online 28 January 2022

2666-0334/© 2022 The Authors. Published by Elsevier Ltd. This is an open access article under the CC BY license (<http://creativecommons.org/licenses/by/4.0/>).

the Ellsworth Mountains range from the present day, through Late-Quaternary glacial cycles (Hein et al., 2016a) to 1.4–3.5 Ma (Sugden et al., 2017), whilst in the Sør Rondane Mountains in Queen Maud Land exposure ages span hundreds of thousands of years (15–659 ka)

(Akçar et al., 2020). In certain situations, it has been shown that the surface debris comprising a blue-ice moraine (BIM) has been derived from the base of the ice (Kassab et al., 2020). Evidence of a subglacial source for this debris has included lithological relationships in which

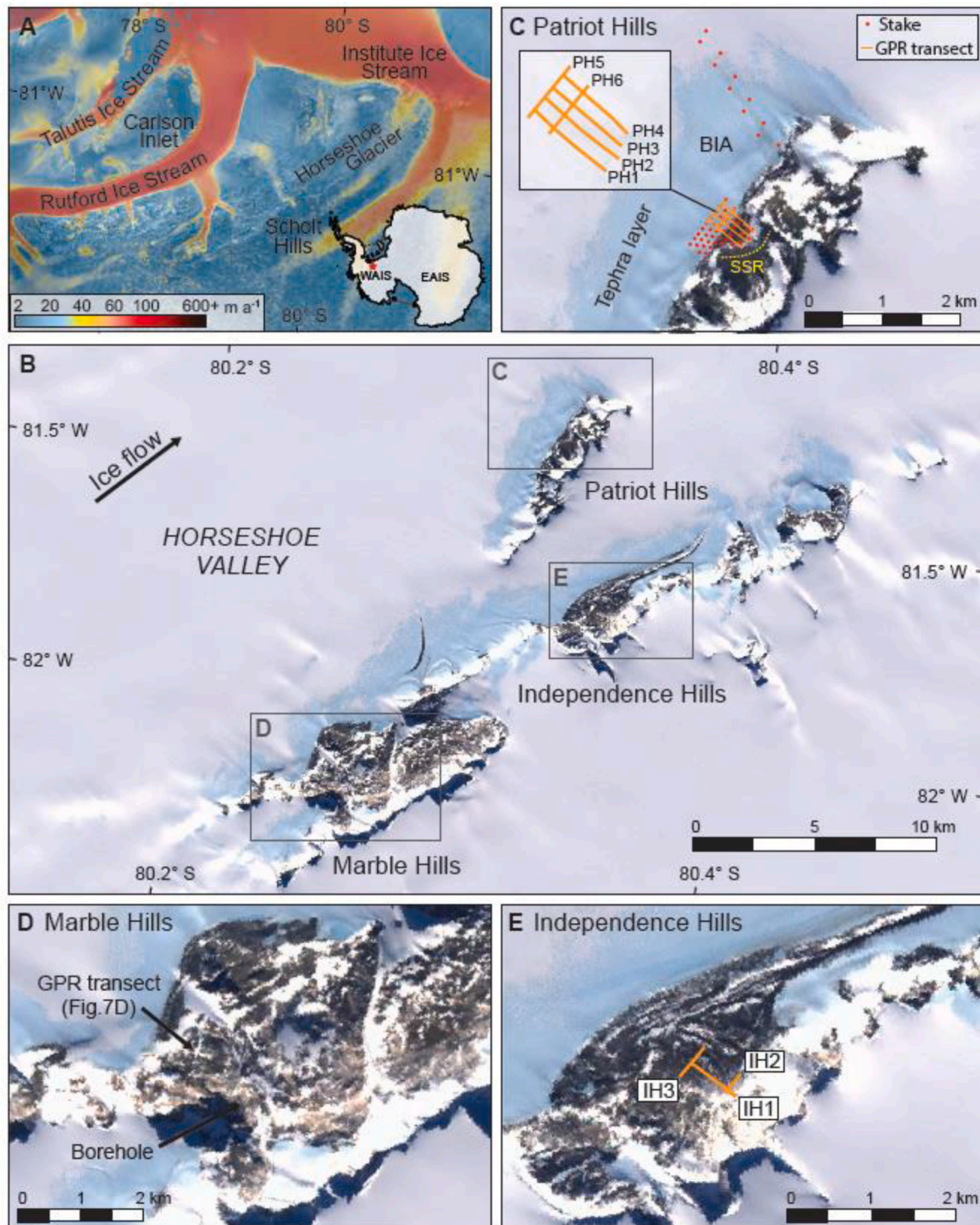


**Fig. 1.** A. Horseshoe Valley field site in West Antarctica. Ice in Horseshoe Valley flows at  $\sim 12 \text{ m a}^{-1}$  (Mouginot et al., 2017; Rignot et al., 2017) towards Institute Ice Stream and the Filchner Ronne Ice Shelf in the Weddell Sea sector of the West Antarctic Ice Sheet (WAIS). B. Location of Patriot, Independence, Marble and Liberty Hills, showing BIA at mountain fronts. Boxes indicate the zoomed in sections in parts C-E of figure. C. Close up of Patriot Hills, showing ground penetrating radar transects along the main embayment (orange lines) shown in Figs. 8 and 9, stakes surveyed for ice flow analysis (red dots) and the location of the sandstone ridge (yellow dotted line) discussed in the text and marked SSR. D. Close up of Marble Hills showing the location of the GPR line shown in Fig. 7D. E. Close up of Independence Hills showing the GPR transects shown in Fig. 10 (orange lines). (For interpretation of the references to colour in this figure legend, the reader is referred to the Web version of this article.)

clasts of bedrock, inferred on geological grounds to lie subglacially, occur on the ice sheet surface (Bader et al., 2017; Palmer et al., 2012) or the isotopic composition of the ice enclosing the debris that demonstrates basal freezing (Graly et al., 2018). Further, geophysical studies at Patriot Hills (Winter et al., 2019) and Mount Acheron in the Transantarctic Mountains (Kassab et al., 2020) have revealed debris bands in ice underlying BIM. In other situations, such as in Heimefrontfjella, Dronning Maud Land, some of the debris may have come from local supraglacial sources (Hättestrand and Johansen, 2005), a situation duplicated in the Sør Rondane Mountains (Akçar et al., 2020).

The focus of this paper is on the moraines that occur on the flanks of glaciers at the foot of the three southerly massifs of the Heritage Range, namely Patriot, Independence and Marble Hills. This site was chosen because (1) the BIA exist on the north-eastern flank of mountains and escarpments lying perpendicular to ice flow from the central West Antarctic Ice Sheet (WAIS) (Fig. 1), unlike many other parts of the Ellsworth Highlands, making them perfect dipsticks for studying the stability and persistence of the WAIS through glacial cycles; (2) The mountains are at the end of the Heritage Range, where the fast flowing Independence and Ellsworth Trough outlets coalesce with the main trunk of the Institute Ice Stream, making their location more likely to record changes in the broader WAIS than other in-mountain BIA in the Heritage Range; (3) there is evidence for dynamic change, switching and mass change in the Institute Ice Stream (Winter et al., 2015) which may be recorded in these BIM; and 4) previous studies suggest erratics are numerous, easily accessible across the mountain ranges and are high in quartz content, supporting cosmogenic exposure dating. The mountains experience persistent katabatic winds flowing down the ice-sheet ice dome from the south and southwest (De Keyser, 2004). The BIA extend ~1.5 km from the mountain foot onto the surface of south-eastward-flowing Horseshoe Glacier and adjacent, smaller outlet glaciers partly fed by ice flowing through or across the mountains (Rivera and Oberreuter, 2014). A previous project in Patriot Hills based on cosmogenic nuclide exposure dating led to the hypothesis that the BIM were formed by the upward movement of debris from the glacier base (Fogwill et al., 2012). The hypothesis was based on surface features, such as the presence of striated clasts, and the emergence of rocks parallel to debris bands on the blue-ice surface. The apparent volume of debris in the ice implied a long period of formation, a conclusion now backed up by a >1.4 Ma record of blue-ice persistence in the three massifs (Hein et al., 2016a). A further discovery is that in the Heritage Range the ice sheet has thinned by ~400 m since 10ka - although it has been close to its present elevation for 3.5 ka (Hein et al., 2016b), possibly thickening modestly in the same period (Bradley et al., 2015; Wolstencroft et al., 2015).

However, key questions remain about BIM in the Heritage Range: 1) What are the processes forming the BIM? 2) What is the rate of formation? 3) Can a better understanding of the process and rate of formation here help our interpretation of the puzzling scatter of cosmogenic ages frequently experienced when dating moraines in Antarctica more generally (Ackert et al., 2007; Balco et al., 2014; Hein et al., 2014), leading to better understanding of ice-sheet evolution and WAIS history? To answer these questions, we employed an integrated geophysical and field glaciology approach focussed on Patriot Hills, also including evidence from Marble and Independence Hills in the southern Heritage Range, West Antarctica in the austral summers of 2012–13 and 2013–14.

## 2. Study area

The Heritage Range is located near the edge of the grounded WAIS dome (Fig. 1). To the northeast the inner grounding line of the Filchner-Ronne Ice Shelf is some 50 km distant. The elevation of the ice on the coastal flank of the mountains is ~800 m while on the inland flank it is ~1200 m. Horseshoe Glacier at the southern end of the Heritage Range occupies a trough extending 1300 m below sea level, where ice in the

centre of the valley is > 2000 m thick (Rivera et al., 2010). Another smaller trough, ~ 800 m below sea level, separates Patriot Hills from the main mountain massifs of Independence and Marble Hills (Casassa et al., 2004; Winter et al., 2016; Winter et al., 2019).

The three mountain massifs are built of tilted marble and limestone conglomerates overlain by greywackes and shale, sandstone and quartzite (Webers et al., 1992). The geometry of this latter arrangement means that quartz-rich erratics occur mostly in the northwest and are carried south-eastward and deposited on the shales and limestones of the three massifs. Climatically, the mean annual temperature at Patriot Hills is estimated to be -28 °C (Dahe et al., 1994) with a net accumulation rate for the wider area in 1996–97 of 7 g cm<sup>-1</sup> a<sup>-1</sup> (Casassa et al., 2004). The rate of ice ablation in the BIA is in the order of 15–20 cm water equivalent per year (Bintanja, 1999; Casassa et al., 2004). Persistent katabatic winds measured near the blue-ice blow from the SSW (De Keyser, 2004). Snow-Blow model outputs (Mills et al., 2019) show that these winds are responsible for creating and maintaining the BIA on the leeward slopes of Patriot Hills and other local mountain fronts. Meteorological data from Patriot Hills reveal 47 warm periods at Patriot Hills since 1997 that could cause surface melt (Carrasco, 2018). A maximum ice velocity of 12.7 m a<sup>-1</sup> was measured in the centre of the valley 13 km north of Patriot Hills (Rivera and Oberreuter, 2014).

The Patriot Hills BIM is continuous for over 6 km and varies in width from 10 to 20 m off promontories to more than 1 km in embayments (Fig. 2). The moraine elevation mirrors that of the glacier margin with an overall lowering to the east but with local altitudinal variability of several tens of metres. The moraine stands above the blue ice at the glacier margin which slopes towards the moraine at angles of ~6°. The moraine is approximately the same elevation as the central axis of Horseshoe Glacier. In Marble Hills a BIM occurs on the southern flank of an outlet glacier flowing from the interior at an elevation of ~1400 m and swings round in the lee of the massif at elevations of ~1000 m. It evolves into a medial moraine as it joins other glaciers draining the interior and merges with Horseshoe Glacier. The BIM in Independence Hills is up to 2 km across and abuts the foot of the main summits of Independence Hills. The width of the surface expression of the moraine decreases as it extends 4 km eastwards parallel to the mountain escarpment but with an increasing zone of glacier ice between it and the cliff. Overall, the elevation of the moraine falls eastwards. However, the western end, broken up by crevasses, falls to the west and is associated with a reversal of flow accompanying mid-Holocene thinning (Casassa et al., 2000; Hein et al., 2016b).

## 3. Methods

Two field campaigns at Patriot, Independence and Marble Hills were undertaken in consecutive austral summers. A three-month season ran from December 2012 to February 2013 (Season 1) and was followed by a resurvey visit in January 2014 (Season 2). Our approach was to carry out a detailed set of measurements over two years in an embayment in the Patriot Hills where the BIM is best developed. Elsewhere, in the adjacent Independence and Marble Hills we relied on targeted field observations backed up by geomorphological mapping. Whilst the focus of ground penetrating radar (GPR) surveys to explore the sub-surface of the moraine sequences was, again, in the Patriot Hills blue ice embayment, we also carried out GPR survey of other moraines and debris covered glaciers in the Patriot Hills on moraines in Independence and Marble Hills and along the adjacent flank of Horseshoe Glacier.

In this paper we link: 1) detailed surveys of surface form and sediments from field mapping, including manual and semi-automated sediment particle size analysis and structure-from-motion photogrammetry (to quantify the geomorphology and sedimentology of surficial sediments), with 2) differential global positioning surveys (DGPS) of a surface stake network and Terrestrial Laser Scanning (to quantify contemporary ice and moraine dynamics); 3) multi-high-resolution geophysical surveys of the glacial structure of the moraines and BIA

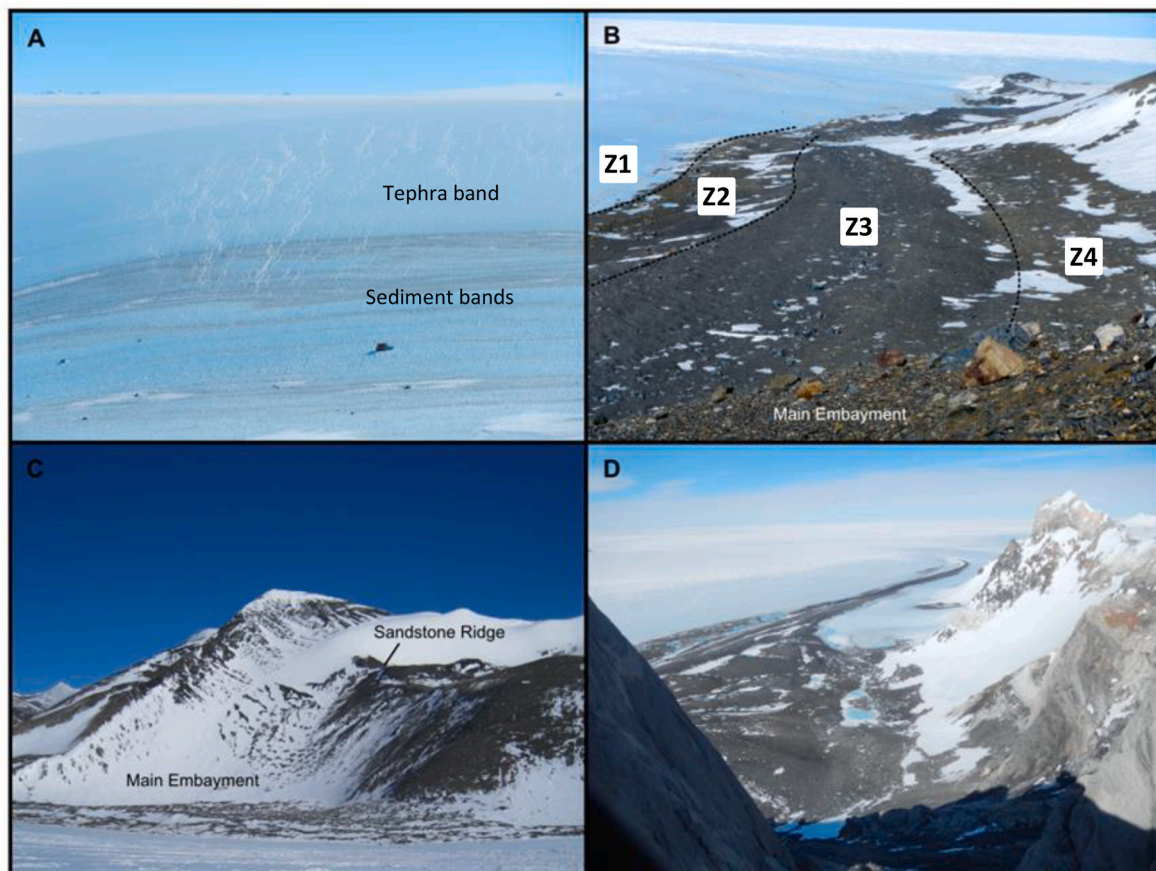


**Fig. 2.** Photographs of the field locations showing A. The BIM zone in front of Patriot Hills where folded debris bands of fine material are visible as well as occasional large erratics. B. The detailed study site at Patriot Hills showing the main BIM zones extending from the blue-ice to the landward flank of the blue-ice embayment (as discussed in the text). C. Looking towards Patriot hills showing the main embayment near the ice margin and the upper basin where a moraine ridge of sandstone clasts is found (labelled Sandstone Ridge). D. The BIM at Independence Hills. Lobes of sediment are incorporated in the fore-field with ridges of sediment extending down glacier. (For interpretation of the references to colour in this figure legend, the reader is referred to the Web version of this article.)

from ground penetrating radar (GPR) (to examine subsurface structure); and 4) cosmogenic nuclide exposure dating of clasts and bedrock to study the timing of sediment delivery to moraine surfaces.

### 3.1. Ice-flow velocity mapping from repeat differential global positioning system

We established a network of stakes on glacier ice and surveyed these using DGPS to establish distal and proximal flow velocity fields (Fig. 1C). Stake positions were surveyed at the beginning of Season 1 and end of Season 2 using a dual-frequency Trimble R4 receiver. Data were corrected using an R4 reference base station positioned on nearby bedrock. Post-processed horizontal and vertical positional uncertainties were  $<0.05$  m and  $<0.10$  m respectively in Season 1, and  $<0.03$  m and  $<0.08$  m in Season 2. Stake movements were used to calculate xy displacement directions and magnitudes between the two surveys. Stake heights above the ice surface were additionally used to quantify surface ablation at Patriot Hills moraine-glacier ice transition.

### 3.2. Ice penetrating radar

A PulseEKKO 1000 ground penetrating radar (GPR) system with 200 MHz antennae was used to survey BIA and associated moraine sequences. Grids of profiles were recorded at Patriot Hills (P1–P6), Independence Hills (IH1–IH3) and single profile on Marble Hills (MH1). To obtain high-resolution profiles the system was set to collect data in step-and-collect mode (Woodward et al., 2001), where data were collected at

0.1 m intervals, with an in-field stack of 8. GPR transects were surveyed for topographic correction using a Trimble DGPS (corrected to decimetre accuracy with a local base station). A standard ice velocity of  $0.168 \text{ m ns}^{-1}$  was applied for depth correction. Processing steps in the commercial radar processing software package ReflexW (Sandmeier Scientific Software, version 7.2.2) included time-zero correction, background removal, high-pass frequency filtering (dewow), bandpass filtering and application of an energy-decay gain to compensate for geometric spreading losses in the radargram (Daniels et al., 2004). As point reflectors (indicative of sediment) are more apparent in unmigrated data, migration was not applied. Opendtect seismic interpretation software (2015) was employed to plot radargrams in real space using DGPS co-ordinates, to enable three-dimensional analysis of GPR data.

### 3.3. High-resolution topographic surveys

The Patriot Hills embayment (Fig. 2B) was surveyed using a Riegl LMS-Z620 terrestrial laser scanner (TLS) in Season 1 and Season 2. Raw 3D point clouds had a point spacing of 0.05 m at 100 m distance. Data were acquired from six locations across the embayment in December 2012; two of these positions were re-occupied on January 9, 2013 and three positions were reoccupied on January 14, 2014. Automatic outlier removal and manual editing of point clouds in Riegl RiSCAN PRO software (v. 1.5.9) were used to improve raw data quality before overlapping scans were merged for each scan date, and then aligned to the December 2012 scan.

Aerial photographs of the embayment at the end of the 2012/2013 season were acquired from a sub-5 kg fixed-wing uncrewed aerial vehicle (UAV) using a 10 MP Panasonic Lumix DMC-LX5 camera. Photographs were acquired at an approximate flying height of 120 m with an effective overlap of 80%. The ground resolution was  $\sim 1$  pixel: 0.07 m. UAV photographs were the primary input to structure-from-motion (SfM) processing, implemented in Agisoft PhotoScan Professional software (v. 1.1.6). Our specific processing parameters are described fully in Westoby et al. (2016). Ground control data were extracted from the TLS dataset from the end of the 2013 field season. The residual project xyz alignment error was 0.03 m. Multi-view stereo methods were used to construct a dense point cloud and 3D change detection methods were applied to the TLS and UAV-SfM datasets to quantify small-scale inter-annual moraine surface evolution.

### 3.4. Moraine surface sedimentology

Surficial moraine sediment was collected from three  $1 \text{ m}^2$  patches on the Patriot Hills BIM. Sediment was dried and dry-sieved in a laboratory to establish the mass fraction of clasts in the range  $-6.0 \phi$  (91 mm) to  $4.0 \phi$  (63  $\mu\text{m}$ ). Laser diffraction (Malvern Mastersizer 2000) was used to determine the grain-size distribution of fractions  $<63 \mu\text{m}$ . For each sample, the length of *a*-, *b*- and *c*-axes were recorded for a representative sample of 50 clasts from the very coarse ( $>32$  mm), coarse (16–32 mm) and medium gravel (8–16 mm) fractions. Roundness was recorded using a modified Powers' (1953) chart. Clast shape was analysed by plotting the RA index (% angular and very angular clasts) against the  $C_{40}$  index (% clasts with a *c/a* axis ratio of  $\leq 0.4$ ). The grain-size distributions of a further nine  $1 \text{ m}^2$  patches was established through the application of digital photo-sieving to orthophotographs derived from terrestrial SfM photogrammetry (Westoby et al., 2015). A relationship between patch-scale surface roughness and median ( $D_{50}$ ) grain size was established and applied to the moraine-scale UAV-SfM model, thus producing a spatially distributed map of  $D_{50}$ , and from which boulder clusters could also be automatically extracted.

The lithology of boulders  $>0.5$  m across was recorded along the same transect in the centre of the main Patriot Hills embayment. On the moraine we examined boulders within a radius of 10 m of selected sites. On the ice surface we examined boulders within 20 m of the BIM margin.

### 3.5. Cosmogenic nuclide dating

To constrain the age of BIM sediments in Patriot and Independence Hills, we measured cosmogenic  $^{10}\text{Be}$ ,  $^{26}\text{Al}$  and  $^{36}\text{Cl}$  in locally derived limestone blocks and erratic quartz-bearing boulders and cobbles. A portable angle grinder, hammer and chisel were used to sample the top few cm of boulder surfaces away from sharp edges. Wet chemistry was conducted at the University of Edinburgh's Cosmogenic Nuclide Laboratory following the methods described by Hein et al. (2016a) and Marrero et al. (2018). Accelerator Mass Spectrometry (AMS) measurements were conducted at the Scottish Universities Environmental Research Centre (SUERC) AMS Laboratory in East Kilbride, UK. For exposure age calculations we used default settings in Version 2.1 of the CRONUScalc programme (Marrero et al., 2016b) and the CRONUS-Earth production rates (Borchers et al., 2016; Marrero et al., 2016a; Phillips et al., 2016) together with the nuclide-dependent scaling of Lifton-Sato-Dunai (Lifton et al., 2014). The exposure ages presented do not include corrections for rock surface erosion, snow cover, or production rate variations caused by elevation changes associated with glacial isostatic adjustment (GIA) and/or ice sheet thinning through time. In the case of the latter two issues, any GIA adjustment is low (Bradley et al., 2015), but the ice surface has lowered by at least 250 m in the last 10 ka (Hein et al., 2016b), and this could make apparent exposure ages erroneously old. Information on sampling, production rates, assumptions, and full sample chemistry can be found in Tables 1 and 2.

## 4. Results

As data collection was focused in the main embayment at Patriot Hills, many of the results describe this BIM. Other results are presented from Independence Hills and Marble Hills. Here we refer to the Heritage Range BIM as BIM found on the three sets of hills mentioned above. We first present ice flow data and geomorphological studies at the Patriot Hills main embayment in Section 4.1 and 4.2. We then present broader sedimentological data collected across the Heritage Range in Section 4.3, the impact of buried ice in Section 4.4, Sections 4.5 and 4.6 explore erratic trains and periglacial processes in the Patriot Hills BIM, before the results sections 4.7 and 4.8 cover englacial structure and cosmogenic exposure dating across the Heritage Range.

### 4.1. DGPS records of ice sheet motion at Patriot Hills

Velocities measured  $>2.5$  km from Patriot Hills show ice flow approximately parallel to the main front of the massif (Fig. 3A–C), following the main flow of Horseshoe Glacier. Repeat measurements of stakes show that velocity increases with distance from the mountains, with flow speeds of  $5\text{--}10 \text{ m a}^{-1}$  4 km away from Patriot Hills, and  $\sim 1 \text{ m a}^{-1}$  2.5 km from the mountain front. Closer to the mountain front flow is reoriented towards Patriot Hills. Again, flow rates decrease towards the ice sheet margin, from  $\sim 0.4 \text{ m a}^{-1}$  to  $\sim 0.2 \text{ m a}^{-1}$ . These ice flow vectors reflect the slow flowing ice of Horseshoe Glacier consistent with the current cold-based ice conditions at the ice sheet margin. Flow vectors on the moraine surface overlying glacier ice appears more chaotic, but in reality, differences in DGPS measurements recording change in the region of  $0.1 \text{ m a}^{-1}$  are below the level of detection achievable and comparable to error levels for surveys in complex topography at high latitudes (where satellites are seldom nadir) so cannot be used to discern a clear flow signal.

### 4.2. Blue-ice moraine geomorphology at Patriot Hills

The geomorphology of Patriot Hills BIM embayment reveals four landscape types displayed by the BIM and their relative importance varies from site to site (Fig. 2). Zone 1, comprising the ice surface adjacent to the margin, is a source of debris in folded bands and/or isolated boulders separated by clear ice (Figs. 2A and 3D). In embayments the surface exposure of debris bands may extend hundreds of metres from the ice margin. On promontories the ice slope is steepest and the debris bands are concentrated near the ice margin. Zone 2, adjacent to the ice margin is a pitted ramp or ridge covered thinly with debris and rising gently with distance from the ice margin. The zone is marked by ablation basins (Fig. 4A), as well as large boulders standing proud of the surface on pedestals of ice. Such a zone is commonly 10s–100s of metres wide. A third landscape type, Zone 3, consists of boulder-rich ridges, 1–10s of metres high, extending for km parallel to the ice margin on the landward side of the pitted ablation zone. Arcuate, longitudinal main moraine crests are disrupted by transverse linear grooves. The grooves show a splaying pattern as they extend into the embayment, and some overlie the site of tensional fractures in the underlying ice (Fig. 4B). Large boulders  $>0.5$  m in diameter are concentrated within the moraine complex and are especially dense along the main ridge in Zone 3 and near the ice margin in Zone 2 (Fig. 4C). The final landscape type, Zone 4, is a more subdued landscape with evidence of ablation hollows and ridges but with gentler slopes and a continuous debris cover. This landscape type occurs on the landward side of the BIM complex.

The moraine ridges both close to, and far from, the ice margin emerge as axes of activity and relative uplift (Fig. 5A). This activity is not simply confined to 'inward' or 'outward' movement of moraines within the embayment, but also involves a lateral component. Areas of seemingly persistent uplift of  $0.10\text{--}0.15 \text{ m a}^{-1}$  during the summer season in 2012/2013 were located on the ice-distal face of the main moraine

**Table 1**  
 Rock sample details and cosmogenic nuclide concentrations for erratics and local boulders from the Heritage Range. Samples are divided by location (Marble, Independence, and Patriot Hills). Relevant location and sample information is provided along with the appropriate cosmogenic nuclide concentrations ( $^{10}\text{Be}$ ,  $^{26}\text{Al}$ , and/or  $^{36}\text{Cl}$ ) for each sample. RF denotes rockfall.

BI Zone	Sample ID	Lat.	Long.	Alt.	Lithology*	Thickness	Topo shielding	Quartz mass	$^{10}\text{Be}$ AMS ID <sup>a</sup>	$^{10}\text{Be}$ concentration <sup>b</sup> ± 1σ	$^{26}\text{Al}$ AMS ID <sup>a</sup>	$^{26}\text{Al}$ concentration <sup>c</sup> ± 1σ	$^{36}\text{Cl}$ AMS ID <sup>a</sup>	$^{36}\text{Cl}$ concentration <sup>d</sup> ± 1σ	Total Cl concentration <sup>e</sup> ± 1σ
		(dd)	(dd)	(m asl)		(cm)		(g)		( $10^3 \text{ atom g}^{-1} [\text{SiO}_2]$ )		( $10^3 \text{ atom g}^{-1} [\text{SiO}_2]$ )		( $10^3 \text{ atom g}^{-1} \text{ sample}$ )	(ppm)
<b>Marble Hills</b>															
1	MH12-451	-80.2529	-82.0915	879	SS	4.0	0.999	26.538	b7355	10.19 ± 1.99	a1852	51.77 ± 7.47	-	-	-
1	MH12-471	-80.2533	-82.0868	869	SS	3.5	0.998	18.711	b7356	0.20 ± 1.66	a1853	12.65 ± 6.62	-	-	-
1	MH12-421	-80.2529	-82.1038	867	SS	6.0	0.998	22.569	b8390	6.23 ± 2.03	na	na	-	-	-
2	MH12-553	-80.2894	-82.0395	727	SS	5.0	0.991	27.253	b8394	271.25 ± 9.61	a2152	1812.96 ± 90.58	-	-	-
4	IH12-13	-80.3561	-81.6695	865	Qtz SS	5.0	0.996	21.218	b9844	26.16 ± 5.20	na	na	-	-	-
4	IH12-14	-80.3560	-81.6702	861	Congl.	5.0	0.996	30.135	b7357	38.09 ± 2.70	a1856	295.44 ± 17.98	-	-	-
2	IH12-212	-80.3528	-81.6605	857	Qtzite	3.0	0.997	29.053	b8385	472.70 ± 16.24	a2143	3868.44 ± 151.30	-	-	-
2	IH12-222	-80.3527	-81.6609	856	Red SS	4.0	0.997	24.833	b9845	182.83 ± 7.15	na	na	-	-	-
3	IH12-192	-80.3549	-81.6608	865	Marb.	1.0	0.996	-	-	-	-	-	c2801	3249 ± 42	3.4 ± 0.3
3	IH12-202	-80.3552	-81.6600	867	LS	3.0	0.996	-	-	-	-	-	c2802	1899 ± 50	20.5 ± 1.3
RF	IH12-24	-80.3536	-81.7184	865	LS	3.0	0.942	-	-	-	-	-	c3234	896 ± 40	20.5 ± 2.3
RF	IH12-25	-80.3562	-81.7187	861	Marb.	2.0	0.936	-	-	-	-	-	c3235	684 ± 32	10.7 ± 2.0
RF	IH12-27	-80.3552	-81.6993	861	Marb.	4.5	0.985	-	-	-	-	-	c3236	8814 ± 366	3.0 ± 1.9
RF	IH12-29	-80.3581	-81.6968	837	Marb.	3.0	0.956	-	-	-	-	-	c3237	886 ± 40	7.8 ± 2.0
1	PH12-971	-80.3303	-81.2901	738	Qtz SS	3.0	0.997	23.031	b8371	0.79 ± 1.17	na	na	-	-	-
1	PH12-1331	-80.3200	-81.4135	762	SS	3.0	0.995	25.651	b8379	8.92 ± 1.51	na	na	-	-	-
1	PH12-961	-80.3300	-81.2939	742	SS	3.5	0.997	27.098	b7334	13.49 ± 2.25	a1834	67.80 ± 8.25	-	-	-
1	PH12-1451	-80.3252	-81.3540	751	SS	5.0	0.996	25.949	b7337	15.24 ± 2.33	a1838	107.36 ± 10.64	-	-	-
1	PH12-160	-80.3252	-81.3540	751	SS	5.0	0.995	6.916	b10083	0.08 ± 2.03	na	na	-	-	-
1	PH12-102	-80.3308	-81.2938	742	SS	6.0	0.996	26.541	b8372	15.21 ± 1.95	a2132	154.58 ± 15.63	-	-	-
1	PH12-169	-80.3277	-81.3298	759	Qtzite	3.0	0.995	22.538	b10085	8.90 ± 0.95	na	na	-	-	-
2	PH12-165	-80.3269	-81.3441	754	Red SS	3.0	0.995	31.044	fail	na	a1839	115.98 ± 22.70	-	-	-
2	PH12-77	-80.3252	98.6362	757	LS	0.7	0.989	-	-	-	-	-	c2792	2270 ± 89	29.7 ± 2.4
2	PH12-164	-80.3272	-81.3425	754	SS	6.0	0.995	14.516	b10084	2.23 ± 1.16	na	na	-	-	-
2	PH12-170	-80.3280	-81.3302	764	Qtzite	3.0	0.995	26.321	b8384	4.67 ± 1.43	a2142	6.24 ± 9.09	-	-	-
2	PH12-74	-80.3258	98.6437	764	LS	2.5	0.994	-	-	-	-	-	c2790	1016 ± 32	25.1 ± 1.8
2	PH12-105	-80.3316	-81.2928	743	Red SS	1.5	0.996	25.642	b8373	530.67 ± 16.89	a2133	3924.37 ± 195.25	-	-	-
3		-80.3281075973063	-81.3386942166835	770	Calcite	2.0	0.993	-	-	-	-	-	c3045	375 ± 10	28.4 ± 0.1

(continued on next page)

Table 1 (continued)

BI Zone	Sample ID	Lat. (dd)	Long. (dd)	Alt. (m asl)	Lithology*	Thickness (cm)	Topo shielding	Quartz mass (g)	<sup>10</sup> Be AMS ID <sup>a</sup>	<sup>10</sup> Be concentration <sup>§</sup> ± 1σ (10 <sup>3</sup> atom g <sup>-1</sup> [SiO <sub>2</sub> ])	<sup>26</sup> Al AMS ID <sup>a</sup>	<sup>26</sup> Al concentration <sup>#</sup> ± 1σ (10 <sup>3</sup> atom g <sup>-1</sup> [SiO <sub>2</sub> ])	<sup>36</sup> Cl AMS ID <sup>a</sup>	<sup>36</sup> Cl concentration <sup>§</sup> ± 1σ (10 <sup>3</sup> atom g <sup>-1</sup> sample)	Total Cl concentration <sup>§</sup> ± 1σ (ppm)
3	PH12-158	-80.3318	-81.2953	738	Red SS	3.0	0.991	31.059	b8374	510.57 ± 24.92	a2134	3661.80 ± 226.62	-	-	-
3	PH12-106	-80.3260	98.6390	774	Calcite	2.0	0.989	-	-	-	-	-	c2791	539 ± 86	111.6 ± 22.6
3	PH12-156	-80.3283	-81.3411	764	SS	3.0	0.989	27.647	b10081	747.43 ± 23.22	na	na	-	-	-
3	PH12-155	-80.3282978665083	-81.3411696441471	766	LS	3.0	0.989	-	-	-	-	-	c3044	2181 ± 55	51.5 ± 0.2
3	PH12-157	-80.3279	-81.3480	763	SS	4.0	0.989	25.219	b10082	98.98 ± 3.65	na	na	-	-	-
4	PH12-152	-80.3286	-81.3434	761	Red SS	4.0	0.985	25.684	b8383	437.98 ± 13.18	a2141	3361.50 ± 138.50	-	-	-
4	PH12-148	-80.3289	-81.3430	763	Qtz SS	4.5	0.985	31.316	b10076	494.19 ± 15.48	na	na	-	-	-
4	PH12-146	-80.3289	-81.3455	770	Red SS	3.0	0.985	23.049	b10075	48.68 ± 1.95	na	na	-	-	-
4	PH12-153	-80.3286	-81.3511	764	Qtzite	3.0	0.987	6.101	b10078	347.17 ± 11.60	na	na	-	-	-
RF	PH12-79	-80.3241	278.6172	771	LS	1.5	0.992	-	-	-	-	-	c2798	673 ± 30	40.2 ± 3.4
RF	PH12-80	-80.3249	278.6100	844	LS	5.5	0.980	-	-	-	-	-	c2799	2787 ± 73	20.6 ± 1.3
RF	PH12-82	-80.3268	278.6143	865	LS	3.0	0.988	-	-	-	-	-	c3261	617 ± 31	24.0 ± 2.5
RF	PH12-83	-80.3278	278.6209	918	LS	1.8	0.994	-	-	-	-	-	c2800	2643 ± 87	28.5 ± 2.0

\*SS: sandstone; Qtz: quartz; Qtzite: quartzite; Congl.: conglomerate; LS: Limestone; Marb.: Marble or marbleised limestone. Rock density 2.7 g cm<sup>-3</sup>; attenuation length 153 ± 10 g cm<sup>2</sup>. Wet chemistry completed at the University of Edinburgh's Cosmogenic Nuclide Laboratory following established protocols (Hein et al., 2016a; Marrero et al., 2016b, 2018).

<sup>§</sup>Normalised to NIST SRM-4325 Be standard material with a revised nominal <sup>10</sup>Be/<sup>9</sup>Be ratio (2.79 × 10<sup>-11</sup>; Nishiizumi et al., 2007) and half-life of 1.387 Ma (Chmeleff et al., 2010; Korschinek et al., 2010) and corrected for process blanks; uncertainties include propagated AMS sample/lab-blank uncertainty and a 2% carrier mass uncertainty.

<sup>#</sup>Normalised to the Purdue Z92-0222 Al standard material with a nominal <sup>27</sup>Al/<sup>26</sup>Al ratio of 4.11 × 10<sup>-11</sup> that agrees with Al standard material of (Nishiizumi, 2004) with half-life of 0.705 Ma (Xu et al., 2010).

<sup>10</sup>Be and <sup>26</sup>Al concentrations are corrected for process blanks; uncertainties include propagated AMS sample/lab-blank uncertainty and a 2% carrier mass uncertainty and a 3% stable <sup>27</sup>Al measurement (ICP-OES) uncertainty. Process blanks were spiked with 250 μg <sup>9</sup>Be carrier (Scharlau Be carrier, 1000 mg/l, density 1.02 g/ml) and 1.5 mg <sup>27</sup>Al carrier (Fischer Al carrier, 1000 ppm). Samples were spiked with 250 μg <sup>9</sup>Be carrier and up to 1.5 mg <sup>27</sup>Al carrier. Blanks range from 3.3 – 9.3 × 10<sup>-15</sup> [<sup>10</sup>Be/<sup>9</sup>Be]; and 1.6–7.5 × 10<sup>-15</sup> [<sup>26</sup>Al/<sup>27</sup>Al].

<sup>a</sup>A <sup>35</sup>Cl carrier (ORNL batch 150301, 1–2 mg <sup>35</sup>Cl) was added to the sample prior to dissolution. <sup>36</sup>Cl AMS measurements were normalised to the Z93 Purdue standard (assumed <sup>36</sup>Cl/total Cl ratio of 1.2 E-12), with additional Nishiizumi standards (<sup>36</sup>Cl/total Cl ratio of 1.6 E-12 and 5E-13) checked every 10 measurements. The sample was blank-corrected individually based on <sup>36</sup>Cl and total Cl concentrations in the process blanks for that batch of samples and based on the method described in Marrero et al. (2018). Previously published errors in concentrations have been corrected here. Raw data for the Accelerator Mass Spectrometry values, blank subtraction, and carrier information are included in the Supplementary Spreadsheet.

Data previously reported by 1Hein et al. (2016a), 2Hein et al. (2016b), and 3Sugden et al. (2017).

<sup>a</sup> AMS measurements made at Scottish Universities Environmental Research Centre (SUERC).

**Table 2**

Sample composition information for <sup>36</sup>Cl samples, including bulk rock major element composition, bulk rock trace element composition, and target element composition. Blank subtraction percentages for each sample are also included here.

Name	Units	Uncert A <sup>a</sup>	Uncert B <sup>a</sup>	PH12-74	PH12-76	PH12-77	PH12-79	PH12-80	PH12-82	PH12-83	PH12-155	PH12-158	IH12-24	IH12-25	IH12-27	IH12-29
Uncert <sup>a</sup>	–			B	B	A	B	A	A	A	B	A	A	A	A	A
Bulk density	g/cm <sup>3</sup>	0.1	0.1	2.5	2.6	2.5	2.5	2.5	2.5	2.5	2.6	2.5	2.5	2.55	2.55	2.55
SiO <sub>2</sub>	bulk wt %	1.67	0.2	3.19	0.37	4.05	4.64	4.05	4.05	4.05	0.72	4.05	1.89	0.64	0.64	1.89
TiO <sub>2</sub>	bulk wt %	0.04	0.02	0.05	0	0.08	0.08	0.08	0.08	0.08	0.01	0.08	0.04	0.01	0.01	0.04
Al <sub>2</sub> O <sub>3</sub>	bulk wt %	0.03	0.03	0.86	0.13	1.44	1.96	1.44	1.44	1.44	0.09	1.44	0.55	0.13	0.13	0.55
Fe <sub>2</sub> O <sub>3</sub>	bulk wt %	0.17	0.03	0.34	0.13	0.48	0.51	0.48	0.48	0.48	0.23	0.48	0.28	0.15	0.15	0.28
MnO	bulk wt %	0.02	0.01	0.01	0	0	0.01	0	0	0	0.02	0	0.01	0.02	0.02	0.01
MgO	bulk wt %	3.93	0.4	4.42	0.9	8.21	10.31	8.21	8.21	8.21	0.35	8.21	3.14	0.46	0.46	3.14
CaO	bulk wt %	6.3	0.8	48.42	55.9	42.95	39.32	42.95	42.95	42.95	54.7	42.95	51.24	55.56	55.56	51.24
Na <sub>2</sub> O	bulk wt %	0.04	0.03	0	0	0.05	0	0.05	0.05	0.05	0	0.05	0.05	0.03	0.03	0.05
K <sub>2</sub> O	bulk wt %	0.18	0.01	0.25	0.04	0.39	0.43	0.39	0.39	0.39	0.01	0.39	0.17	0.03	0.03	0.17
P <sub>2</sub> O <sub>5</sub>	bulk wt %	0.04	0.04	0	0.01	0	0	0	0	0	0	0	0.03	0.05	0.05	0.03
CO <sub>2</sub>	bulk wt %	0.61	0.4	42.47	43.6	42.62	42.69	42.62	42.62	42.62	43.58	42.62	43.04	43.35	43.35	43.04
Sm	bulk ppm	0.5	0.1	0.4	0.4	0.42	0.42	0.42	0.42	0.42	0.42	0.42	0.6	0.42	0.42	0.42
Gd	bulk ppm	0.57	0.05	0.32	0.38	0.41	0.41	0.41	0.41	0.41	0.41	0.41	0.52	0.41	0.41	0.41
U	bulk ppm	2.53	0.05	0.19	0.55	1.16	1.16	1.16	1.16	1.16	1.16	1.16	0.96	1.16	1.16	1.16
Th	bulk ppm	2.1	0.1	0	0.2	0.58	0.58	0.58	0.58	0.58	0.58	0.58	0.6	0.58	0.58	0.58
Cr	bulk ppm	23	5	0	0	7.4	7.4	7.4	7.4	7.4	7.4	7.4	23	7.4	7.4	7.4
Li	bulk ppm	7	5	0	0	1.4	1.4	1.4	1.4	1.4	1.4	1.4	0	1.4	1.4	1.4
Target K <sub>2</sub> O	tar wt %	0.01	0.01	9.0E-03	3.5E-03	2.7E-03	1.2E-02	4.8E-03	1.2E-02	7.3E-03	2.1E-03	5.6E-03	5.6E-03	2.7E-03	3.9E-03	3.4E-03
Target CaO	tar wt %	2	2	48.4	52.3	53.2	42.7	49.7	52.0	50.6	53.8	52.3	55.2	55.9	55.1	55.1
Target TiO <sub>2</sub>	tar wt %	0.02	0.02	0	0	0	0	0	1.6E-04	0	6.9E-05	7.3E-05	4.8E-05	8.1E-07	4.3E-06	1.0E-06
Target Fe <sub>2</sub> O <sub>3</sub>	tar wt %	0.2	0.2	0.13	0.03	0.08	0.09	0.03	0.10	0.05	0.11	0.05	0.07	0.02	0.02	0.03
<sup>36</sup> Cl Blank sub	%	–	–	0.6%	2.9%	0.3%	1.2%	0.2%	10.6%	0.3%	1.1%	4.2%	7.3%	8.6%	0.7%	7.0%
Total Cl Blank sub	%	–	–	1.2%	0.3%	1.0%	0.8%	1.4%	1.7%	1.0%	0.1%	0.1%	2.0%	3.6%	12.0%	4.9%

Pore water, analytical water, and boron concentrations are all zero. Pressure and attenuation length (153 g/cm<sup>2</sup>) are calculated according to CRONUScalc (Marrero et al., 2016a). Bulk and target Cl concentrations are assumed to be equal. Bulk sample composition was measured on several similar samples and an average value was used for samples of similar lithology due to the low Cl content of the samples.

Bulk rock major elements (SiO<sub>2</sub> through CO<sub>2</sub>) were measured via XRF at the University of Edinburgh, School of GeoSciences.

Bulk rock trace elements (Sm through Li) were measured via ICP-OES at SGS Mineral Services, Inc. (Canada).

Target concentrations were measured via ICP-OES at the University of Edinburgh, School of Chemistry.

<sup>a</sup> Uncertainties (those listed in column A or B as shown in the ‘uncert’ row) were used to calculate the external age uncertainty.

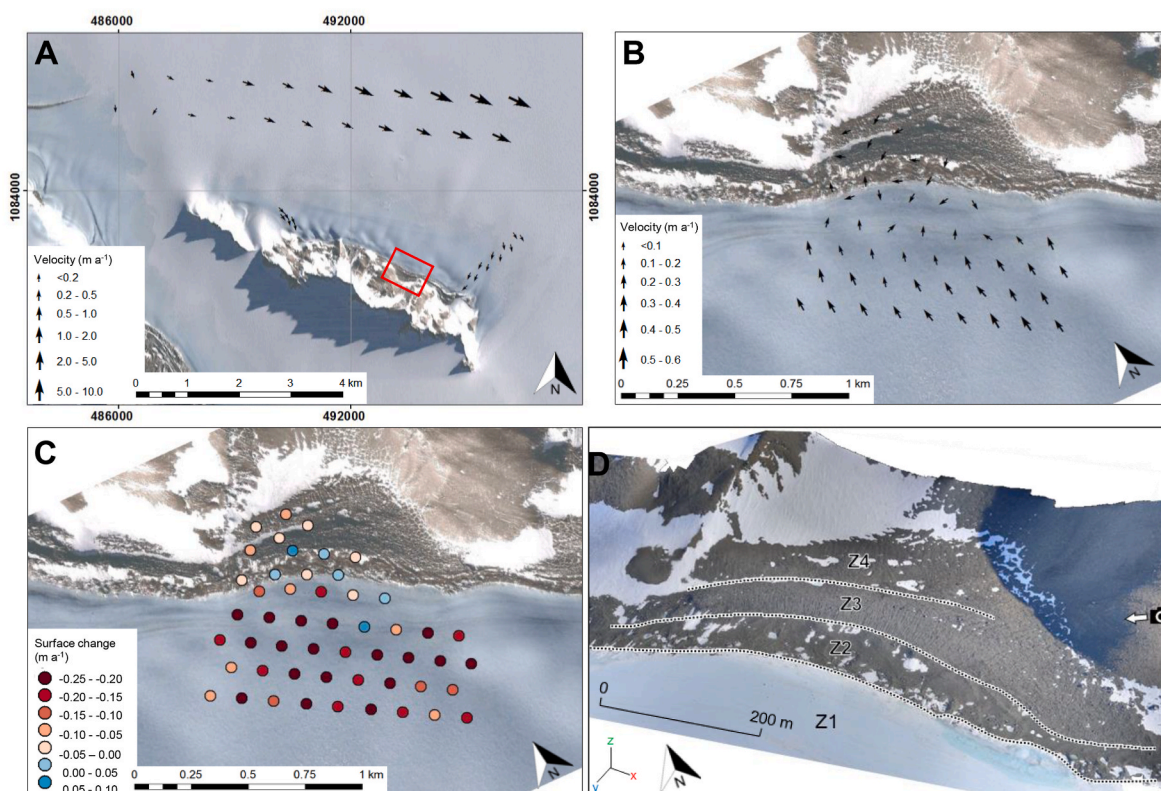


**Fig. 3.** A. Ice flow in the vicinity of Patriot Hills from differential GPS measurements of surface glacio-poles overlaid onto Quickbird imagery. Ice flows faster towards the centre of the Horseshoe Valley. B. Annual horizontal displacements in Patriot Hills BIM embayment show flow vectors curving towards the embayment. Flow close to the margin is slower than the error margin of the technique. C. Annual ablation rates measured at the glacio-poles showing surface lowering of 10–25 cm a<sup>-1</sup> on the ice and less ablation on the moraine. D. Oblique perspective of a UAV-SfM-derived 3D model with orthophotograph drupe of Patriots Hills moraine embayment. Z1–Z4 are morphological zones, where Z1 = glacier ice, Z2 = ice-marginal moraine, Z3 = main moraine crests and Z4 = subdued ridges. The camera position and direction for Fig. 2B are shown for reference.

ridge, as well as along ridges toward the rear of the basin. Surface lowering of 0.05–0.10 m a<sup>-1</sup> occurred at the rear, or landward, extent of the basin within the ablation summer of Season 1 (Fig. 5A) and between the beginning of Season 1 and the end of Season 2 (Fig. 5B). However, there is some overall stability, or even surface uplift of >0.10 m a<sup>-1</sup> in large parts of the moraine from the end of Season 1 to the end of Season 2. There may therefore exist an interplay between moraine uplift and sub-debris ice ablation, whereby the latter dominates during the summer season. Lateral movement within the moraine ridges (Fig. 5B) may reflect lateral extension or ‘stretching’ of the ridges as they encroach into the embayment. Such lateral movement is corroborated from the orientation of splaying crevasse-based grooves in the moraine (Fig. 4B). The landward encroachment of Patriot Hills moraines is likely to result from glacier ice flow into the embayment in compensation for ice ablation within the moraine belt. Overall, the pattern of ablation from summer 2013 to summer 2014 reveals a loss of 0.010–0.25 m a<sup>-1</sup> from the ice surface (Zone 1) and a lesser and more variable pattern on the debris-covered surfaces of the moraines themselves (Zones 2–3).

#### 4.3. Sedimentology of BIM in the Heritage Range

At Patriot Hills the pattern of median grain size measured from the UAV survey represents the distribution of surface clasts over the whole area and shows that the coarser grain sizes occur on the ridges in Zones 3 and 4 as well as in Zone 2 close to the ice margin (Fig. 6A). The dominance of large boulders near the ice edge and on the main ridge in Zone 3 is mapped as red pixels in Fig. 4C and is also clear on the transect in Fig. 6C. Clast orientation for 12 × 1 m<sup>2</sup> patches shows a relationship with local slope (Fig. 6A). Between the ridges, clasts are aligned along the axis of the depression, for example between the two most prominent

ridges and in the depression at the edge of the ice margin. Clasts within patches located on the flanks of the ridges tend to be orientated down-slope. The roundness of the clasts at three sites on the profile across the moraine ridges (a–a’) is dominantly sub-angular and angular (Fig. 6B). Sub-rounded clasts occur as a minority at all sites and become more common on the inland flank of the moraine complex. The finer material from the same sites reveals a coarse till with a median size of coarse sand (–3.5 φ) most clearly displayed close to the ice margin. There is a marked increase in finer material with increased distance from the ice margin.

The lithology counts of the large boulders along the transect shows that the number and variety of exotic rock types is highest on the ice surface and in adjacent Zone 2. Local limestone rocks dominate in the ridges of Zone 3 and are significant in the topographically subdued Zone 4, particularly on the landward flank. Large boulders of quartzite, schist, grey sandstone, red sandstone, shale/slate and marble occur on the ice surface and in Zone 2; here, there are no boulders comprising the local limestone. In contrast 80% of the large boulders on the higher ridges on Zone 3 consist of local limestone, with only 20% comprising exotics. The inner ridge in Zone 4 comprises of 20% local limestone and 80% exotic lithologies.

There are similarities and differences in the lithological relationships between the different massifs in the Heritage Range. BIM in Independence Hills are similar to those in Patriot Hills, in that the ridge furthest away from the mountains front has a wider range and proportion of exotics than the ridges on the inner landward side. Further, several ridges consist wholly of a single rock type of limestone, sandstone or slate. Differences in the make-up of exotic clasts from massif to massif are illustrated by the observation that red sandstone, which is exotic to Patriot Hills and Independence Hills, does not occur in Marble Hills.

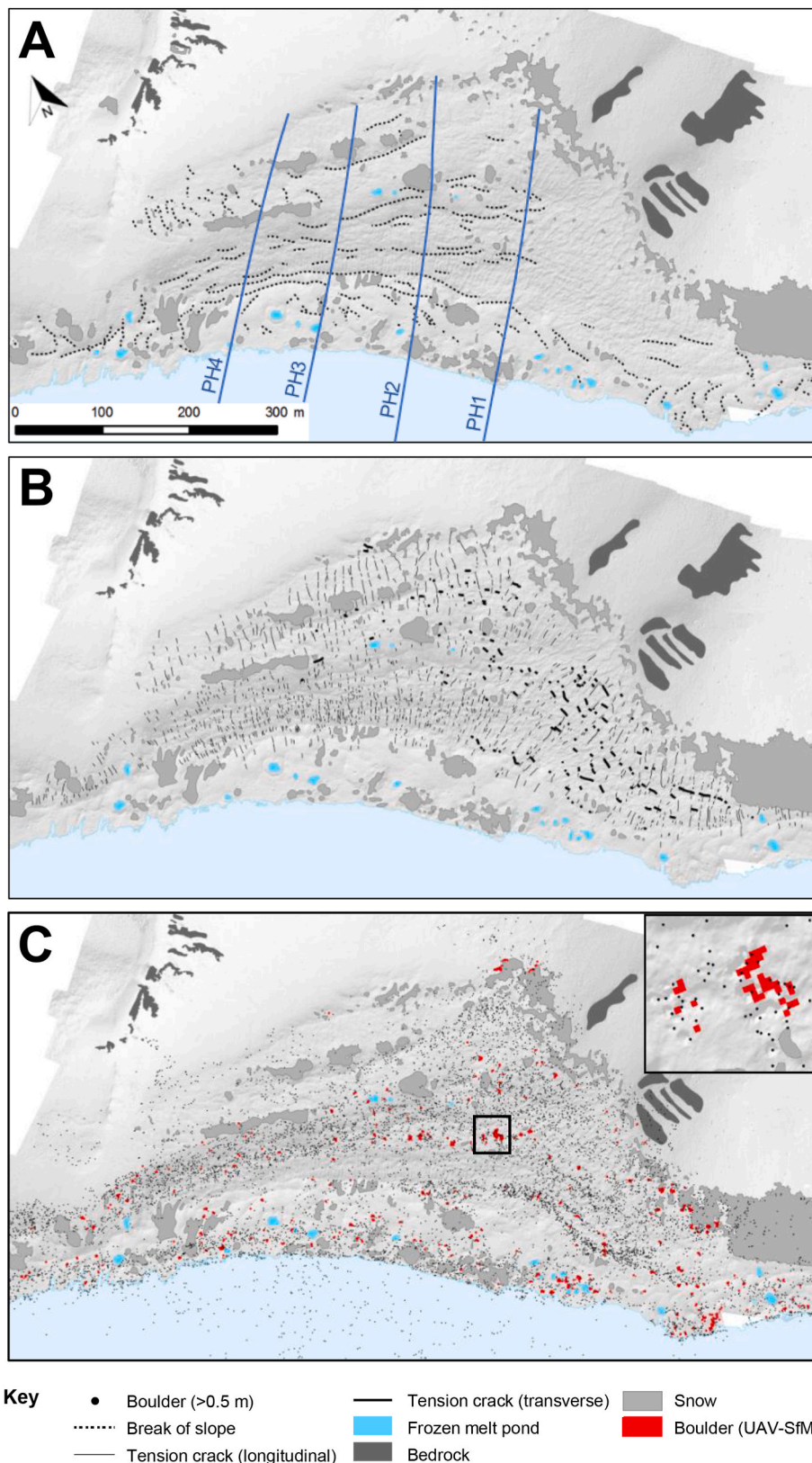


**Fig. 4.** Geomorphology of Patriot Hills BIM complex. A. The location of notable breaks of slope (including moraine crests), melt ponds, and snow patches. The lines of three GPR transects (PH1-PH4), used in Fig. 8 are also shown. B. Transverse and longitudinal tension fractures, showing the majority of fractures running perpendicular to ridge crests. C. mapped distribution of boulders >0.5 m wide from UAV-SfM orthoimagery. Inset panel shows magnification of area highlighted in main panel.

#### 4.4. Buried ice in the Heritage Range

At higher elevations throughout the massifs spreads of relict BIM, formed when the ice sheet elevation was higher in the past, are present. Upon examination, many of the relict moraines and some glacial drift

deposits are underlain by foliated glacier ice (Fig. 7E). In the uplands overlooking the northern part of Marble Hills, up to 7% of the land area is covered in sediments underlain by buried ice. Here the exotic component of the lithology of the clasts is similar to that in the current BIM and reflects deposition by the ice sheet. The buried ice is typically

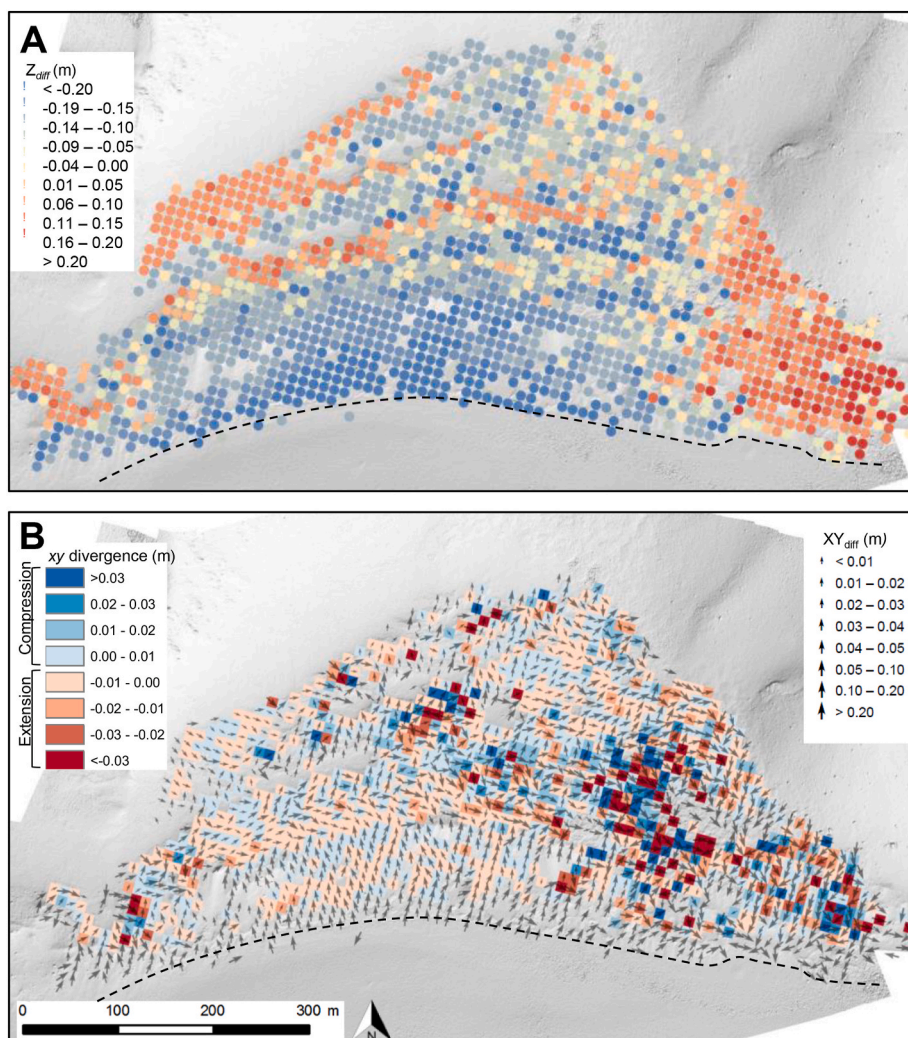


**Fig. 5.** Surface evolution of Patriot Hills BIM embayment. A. Vertical surface change ( $Z_{diff}$ ) from the beginning to end of season 1, derived from 3D differencing of TLS and UAV-SfM topographic datasets. Red areas of relative uplift are found along the ridge crests and to the rear of the moraine where thick sediments protect the ice surface from ablation. B. Horizontal displacement ( $XY_{diff}$ ), displayed as vectors (arrows), and horizontal divergence, representing extension (reds) or compression (blues) of the surface topography from the beginning of Season 1 to Season 2. Ridge crests indicate divergence, with sediments spreading away from the areas of greatest uplift. The thick dashed line indicates the clean ice/moraine covered ice boundary (after Fig. 3c of Westoby et al., 2015). (For interpretation of the references to colour in this figure legend, the reader is referred to the Web version of this article.)

found in low-lying areas or depressions in the landscape and is covered by a thin layer of glacial debris usually 5–20 cm thick. One example of the flow of buried ice is a lobed deposit in the central area of Marble Hills (Fig. 7C). The presence of an ice core with a thickness of ~10–15 m was demonstrated in one location by GPR survey (Fig. 7D). The lobe spans an area from a small saddle, near where the GPR profile was taken, down into a small, internal basin in the central Marble Hills. The arcuate lobe margin and flow ridges are consistent with movement down the local slope. The direction of flow to the south is contrary to the regional direction of ice movement in the past, which was generally towards the east (see Fig. 7C).

A second site showing buried ice overlooks the main embayment in Patriot Hills. A local ice-cored tongue of local limestone material is derived from snow and ice accumulating in the lee of the mountain crest. Its surface is pitted and unstable with enclosed ~30 m basins or kettle holes. The ice-cored tongue cuts across and displaces a distinct elevated moraine ridge parallel to the mountain front and ice-sheet margin (Fig. 2C). The latter moraine can be traced across most of the top of a steep slope and partially around the bounding ridge on the northwest (Fig. 1). The moraine ridge contains exotic red sandstone material, making it distinct from the underlying limestone. The post-depositional timing of the ice movement is supported by the cross-cutting relationship. At some point after the ice sheet had thinned and abandoned the moraine, the buried ice appears to have flowed downhill and displaced a section of the moraine.

#### 4.5. Erratic trains derived from local ice at Patriot Hills

A line of limestone blocks with similar size (0.5–1 m<sup>3</sup>) and lithology, extending some 3 km along the most prominent ridges of the BIM front of Patriot Hills and especially dense in the main embayment, can be traced back to a rockfall source area in a valley now occupied by a local debris-covered glacier (Fig. 7b). This cliffed area would have been progressively exposed as the ice sheet elevation and that of the confluent local glacier lowered. The continuity demonstrates that the local debris-covered glacier transported the boulders downhill and merged them with the BIM at the main ice margin, where they experienced lateral flow to the east (Fig. 7B). The morphology and continuity of the limestone blocks over 3 km suggests they were supplied by multiple smaller rockfalls and experienced continuous transport. Similar erratic trains are seen at Independence and Marble Hills.

#### 4.6. Periglacial slope processes at Patriot Hills

The slopes of Patriot Hills overlooking the current BIM bear minor lobate forms in the regolith characteristic of periglacial slope processes. Our differencing results (Fig. 5) suggest that these debris-mantled slopes are active. Several boulders on such slopes and also on the blue-ice moraines themselves were seen to move between the summer seasons of 2013 and 2014. The implication is that slope evolution on both moraines and the backing slopes is active over annual to intra-annual timescales.

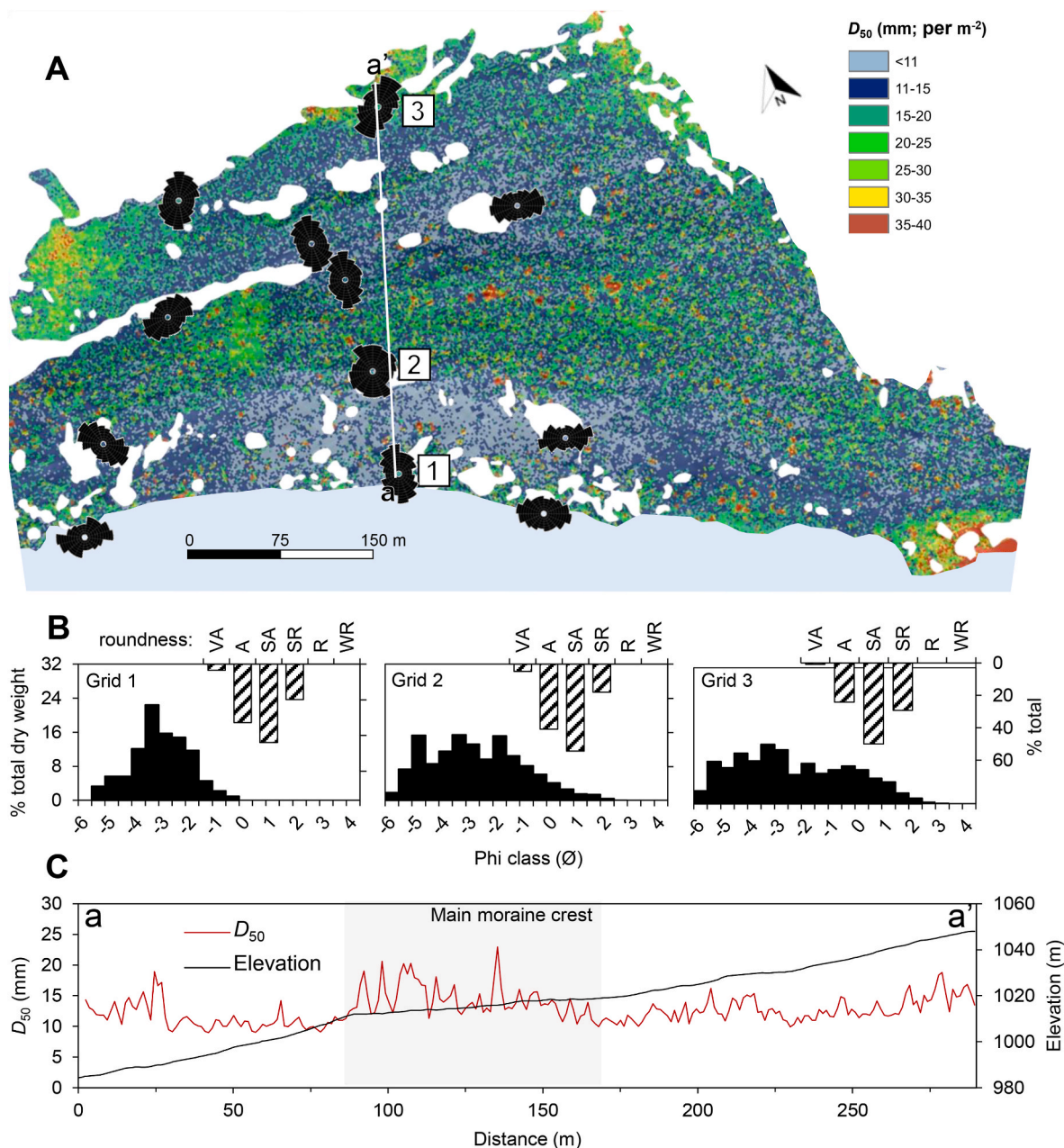


**Fig. 6.** Surface sedimentology of Patriot Hills BIM. A. Distributed grain size distribution mapping from UAV-SfM data (modified from Westoby et al., 2015). Black rose plots show dominant clast orientations for twelve 1 m<sup>2</sup> patches. Profile a-a' shows location of median grain size (D<sub>50</sub>), which appears in panel C. This profile follows GPR line PH3 (see Fig. 4A). B. Results of manual clast analysis (dry-sieving, roundness) for grids 1–3 – see panel A for location. Black bars are % total dry weight, hatched bars show clast roundness distribution. C. Median grain size (D<sub>50</sub>) along the transect (PH3, Fig. 4A). Moraine surface elevation, as extracted from the UAV-SfM data, is also shown. The highest values of median grain size are encountered on the main moraine crest.

A clear example of slope activity involves rock fall onto BIM beneath cliffs. This process is especially common in the case of the cliff-foot moraines of Independence Hills. Here, concentrations of angular boulders of the same lithology and >10 m<sup>3</sup>, lie on the surface of moraines (Fig. 7A). The source of recent rock falls can be identified by scars in the cliffs above.

#### 4.7. Englacial structure in the Heritage Range

The results of step-and-collect GPR transects of Patriot Hills BIA are shown in Fig. 8. Four transects (PH1 – PH4, Fig. 4A) extend from the exposed glacier surface across the moraine zones to the landward flank whilst two transects (PH5 and PH6) crosscut these initial transect lines

(Fig. 8A). PH1 is shown in detail in Fig. 8B, which is annotated in Fig. 8C to highlight subsurface features, where resolution is in the order of 0.1 m) The GPR transects in Fig. 8 show that the slope of the mountain side continues below the moraines and BIA, where ice depth increases from a few metres on the landward flank to >220 m beneath the ice in Zone 1. This slope reflects the edge of the deep Horseshoe Valley trough, noted in airborne radar transects (Winter et al., 2016). Diffuse reflectors at the glacial bed (highlighted in Fig. 8C) suggest that there could be loose sediment beneath the ice, above a glacially eroded bed. Between the exposed glacier ice and the BIM (between Zones 1 and 2) near-surface reflectors in radargram PH1 (Fig. 8B and C) indicate the presence of thin water bodies and ice lenses which have built up over time. Numerous hyperbolic reflectors indicate englacial debris which underlie

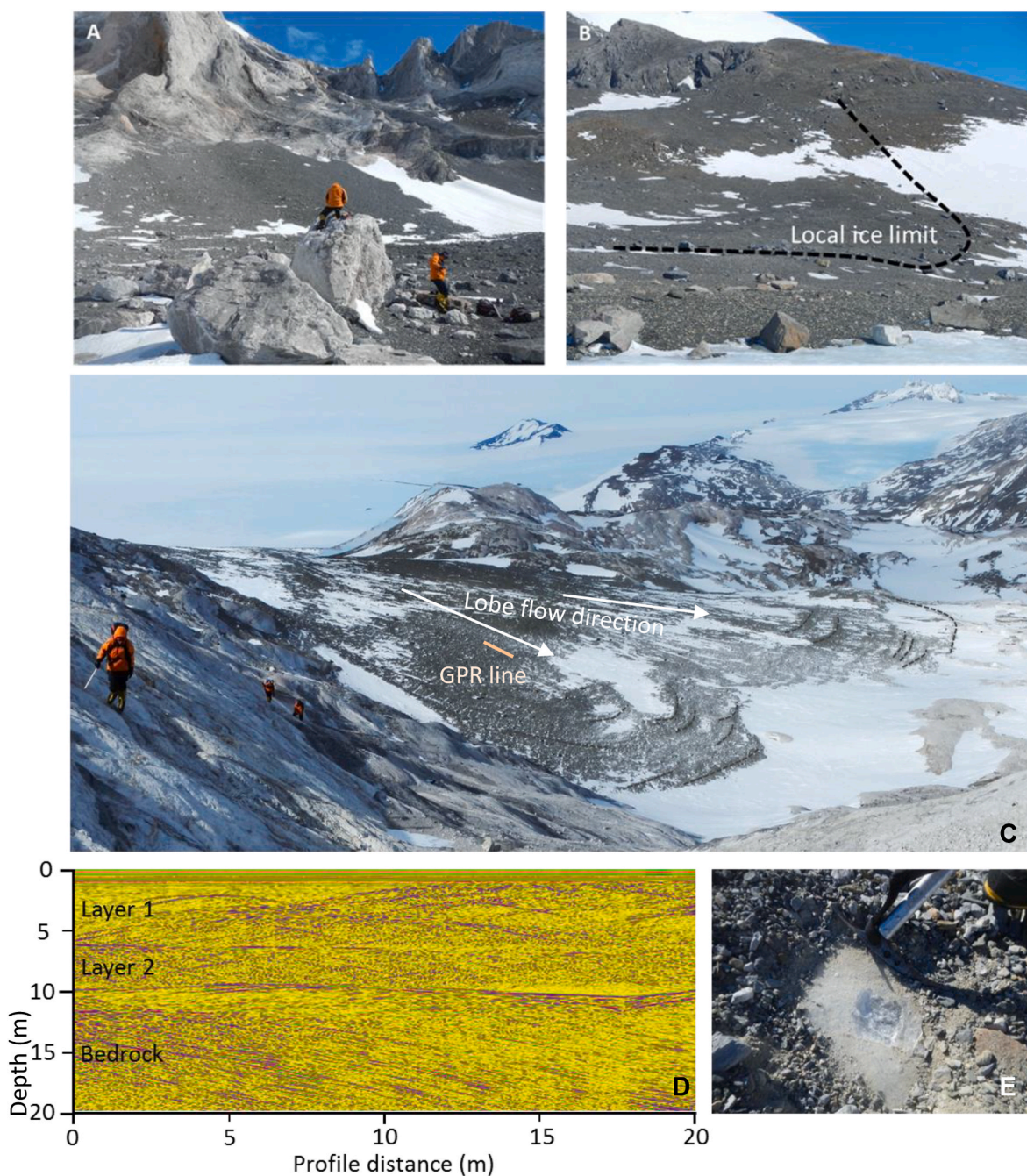


**Fig. 7.** A. Large boulders emplaced onto Independence Hills BIM by rockfall from surrounding slopes.  $^{36}\text{Cl}$  ages suggest early deglacial ages for many of the rockfall blocks of between 11,2 and 15.0 yr BP (sample IH12-25 pictured). B. Lateral moraines, many sourced from the rock cliff in the left distance of Fig. 7B, show local ice limit, and are composed of local limestone boulders in Patriot Hills.  $^{36}\text{Cl}$  ages on the limestone boulders are more scattered than for Independence Hills rockfall blocks, showing some early deglacial exposure ages as well as ages pre-dating the maximum. C. Lobes of the buried glacier ice deposits in Marble Hills with possible post-retreat flow features shown in dashed lines and the location of the GPR line. D. GPR profile across the buried ice deposit, indicating ice depths of up to 10 m. Layers in the ice most likely relate to arcuate thrust plans that produce the lobate moraine shown with the dotted lines. E. A thin veneer of till (10 cm) covers the ice.

the BIM and extend out into the glacier for 200–250 m. The presence of stacked hyperbola points to the existence of dipping bands containing boulders or clumps of debris. Beyond the debris-bearing ice (towards the glacier centreline) steeply dipping reflectors are recorded. These reflectors represent isochrones in the ice, which form through sequential snow deposition.

In Fig. 9 we compare the surface morphology in three zones with the underlying radar reflections. The location of each site is shown in Fig. 8A. The photograph showing boulders and debris bands outcropping on the glacier surface (Fig. 9A) overlies the radar image (Fig. 9D)

that straddles the junction between debris-bearing and debris-free ice. The hyperbola indicating englacial debris are consistent with the presence of englacial boulders that have yet to reach the surface. The steeply dipping reflectors to the left of the image relate to isochrones. An excavation into a high ridge in the boulder-strewn Zone 3 (Fig. 9B) revealed a clump of till surrounded by clear ice. We interpret this as a boudinage structure. Comparison with the underlying englacial structures reveals stacked hyperbola beneath the ridge, a pattern that is consistent with debris that has been stretched and forms a dipping band of boudinage structures (Fig. 9E). It is also possible that some of the

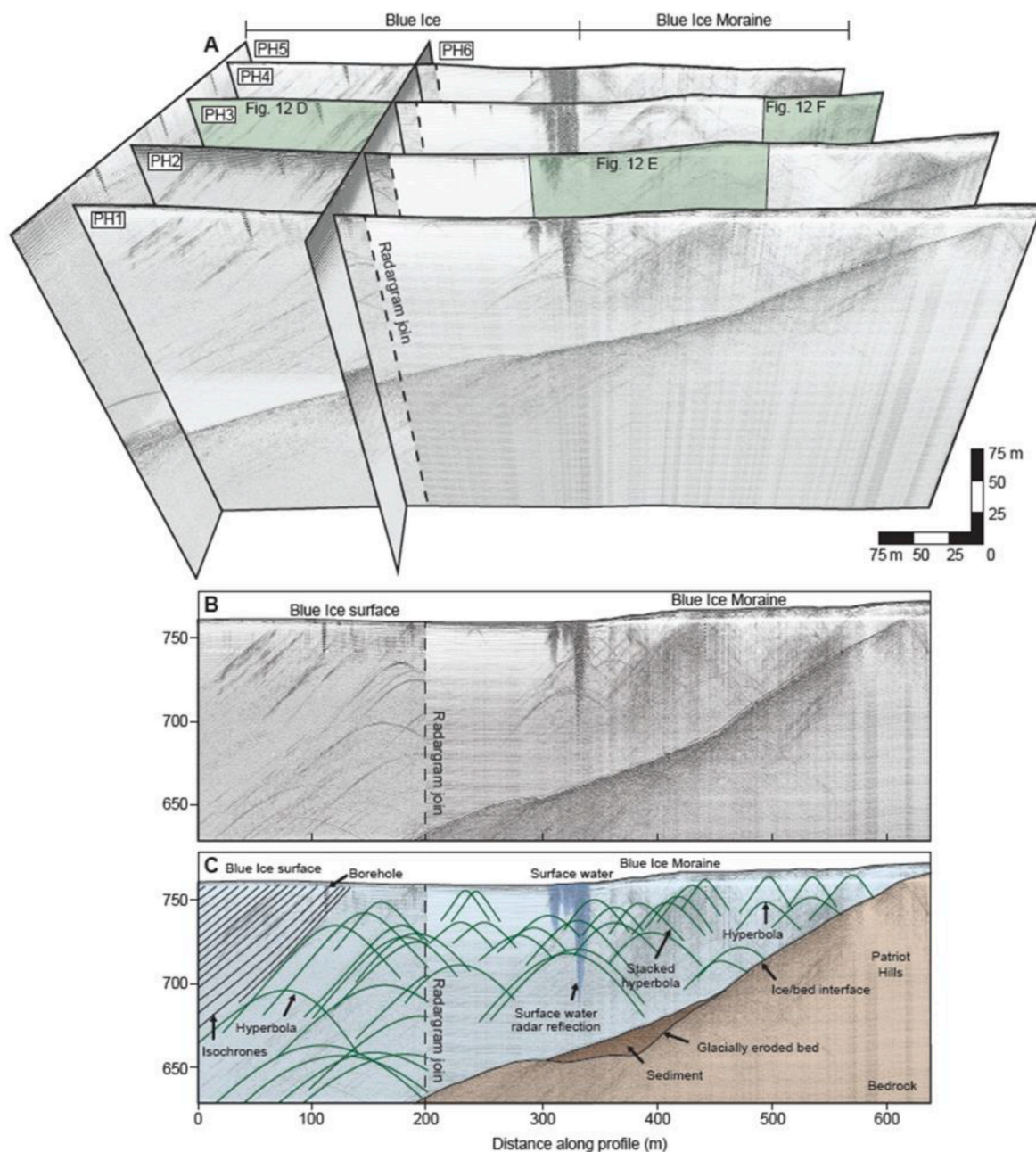


**Fig. 8.** Stop-and-collect GPR transects of Patriot Hills BIA. Survey locations are shown in Figs. 1 and 4. A. GPR grid showing dipping isochrones within Patriot Hills BIA, and Patriot Hills BIM underlain by hyperbolic reflectors from sediment inclusions in the ice. Green boxes denote the location of Fig. 9 D, E and F. B. PH1 GPR line, annotated in C. to show subsurface features, including isochrones, hyperbolic reflectors (representing englacial sediment) and the ice/bed interface. A full description of the features in the figure is given in the text. (For interpretation of the references to colour in this figure legend, the reader is referred to the Web version of this article.)

hyperbola pinpoint the location of boulders. Removal of a thin layer of till at the back of the BIM near the mountain slope reveal fine sediment layers in the surface ice (Fig. 9C). Radar reflections showing dipping debris bands beneath the site suggest this is characteristic of deeper ice at the site (Fig. 9F).

GPR radar transects were also surveyed on the BIM in Independence Hills (Fig. 2D; Fig. 10). In this case we investigated an intricate pattern of arcuate ridges within the moraine complex. The pattern of radar transects is shown in Fig. 10A, with the location in respect of the overall BIM marked in Fig. 10C. The reflections indicate a succession of dipping debris bands, especially clear in radar transect IH3 (Fig. 10A) which was traversed parallel to the trunk glacier between Patriot and Independence Hills. There are also signs of folding of englacial debris in the middle of

transect IH1 (Fig. 10A). The inset radargram (Fig. 10B) shows subsurface reflections across a set of nested arcuate moraines that feature on the surface of the BIM. These reflections suggest that there are discrete remnants of lobes of ice and that each is underlain by a bowl-shaped debris layer. We hypothesize that these lobes represent ice flowing into the moraine complex from hanging valleys in the escarpment of Independent Hills (see Fig. 1). Much of the ice has ablated away leaving their lateral and terminal moraines with their arcuate form. Similar tributary glaciers occur immediately to the southeast where overspilling ice joins the trunk glacier, but in the latter case the mass of ice is sufficient to divert the moraine from the valley side.

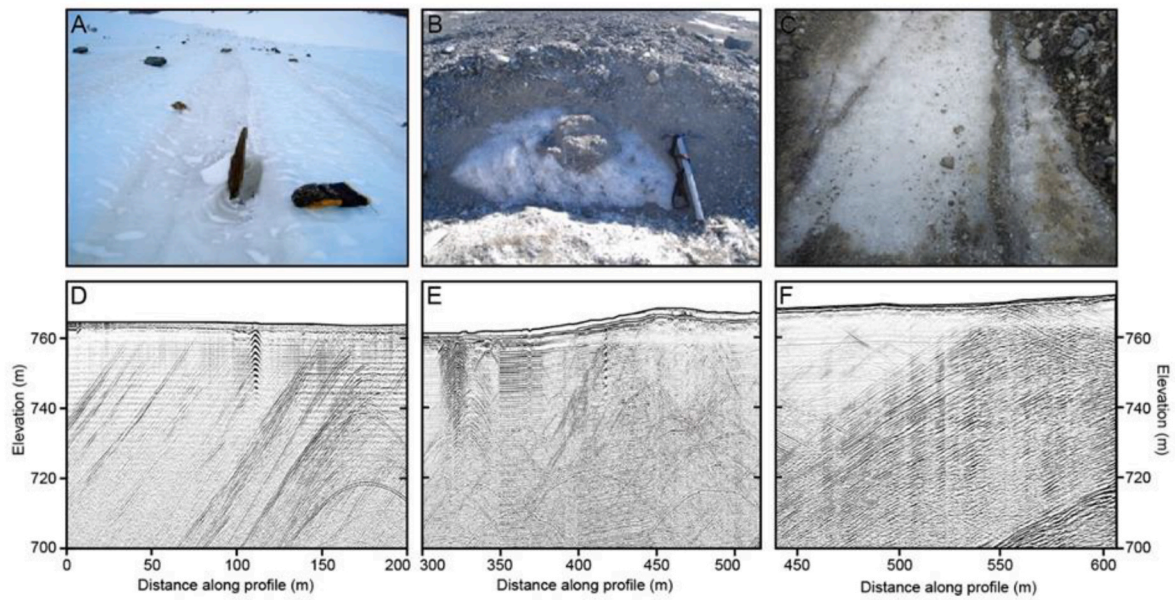


**Fig. 9.** Englacial features of Patriot Hills BIM. A. Emergent debris bands and clasts. B. Sediment inclusions visible in a trench dug through the crest of the BIM. The sediment inclusion indicates boudinage. C. Fine sediment layers within the ice. GPR in panels D–F show the subsurface beneath photographs A–C, detailing steeply dipping isochrones and hyperbolic sediment reflectors. See text for more detail.

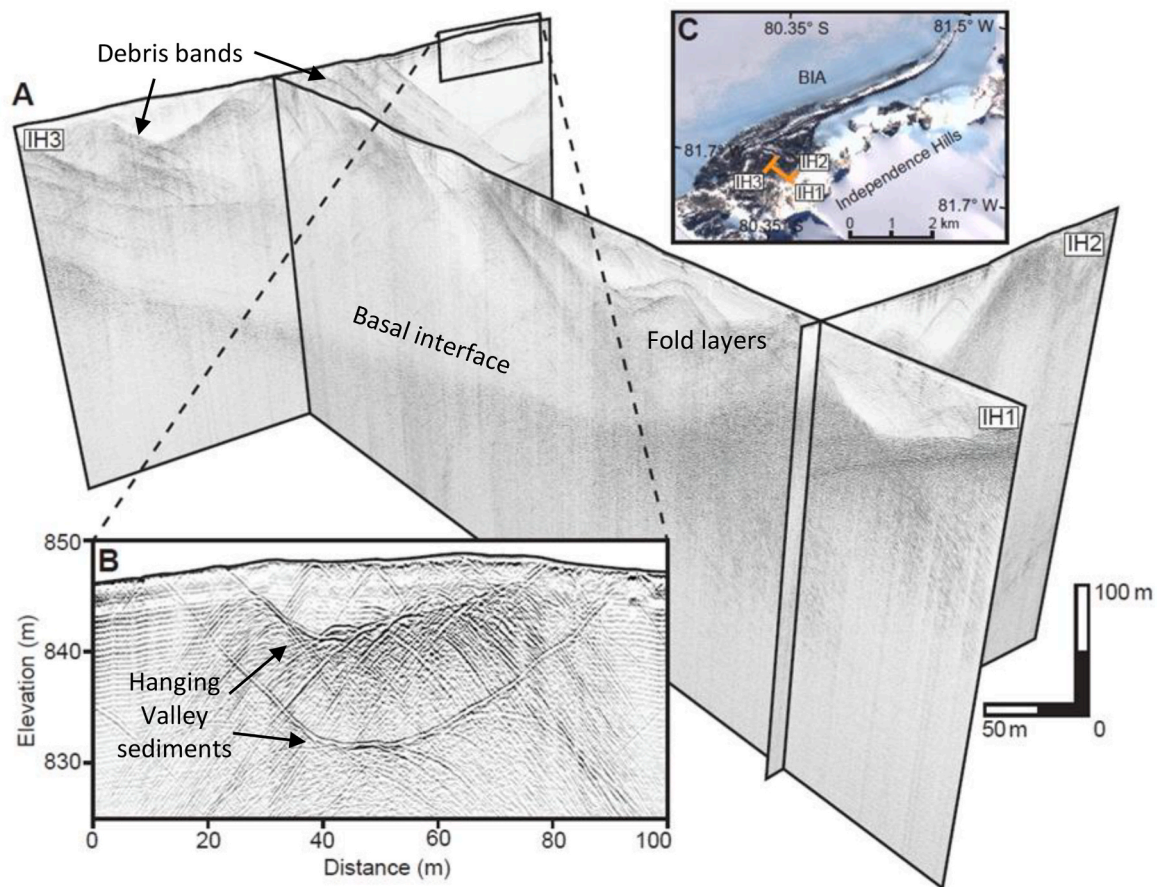


**Fig. 10.** A. GPR transects collected on the BIM sequences in front of Independence Hills (Fig. 2D). The GPR profiles reveal steeply dipping englacial reflectors beneath the surface of the moraine equating to debris bands and possible fold layers. B. Close up of traces collected across a series of nested lobes on the moraine surface. The lobes record basal sediments transported onto the moraine by hanging valleys which have since mostly ablated, leaving their lateral and terminal moraines and ~10 m of ice in the sediment sequence. C. Location of GPR profiles (orange lines) used in A. and B. (For interpretation of the references to colour in this figure legend, the reader is referred to the Web version of this article.)

#### 4.8. Cosmogenic exposure dating

The exposure ages of 23 boulders sampled along GPR transects across the moraine ridges in the Patriot Hill embayment are shown in Fig. 11 and Table 3. Analyses of  $^{10}\text{Be}$  in seven quartz-rich boulders sampled on the ice surface (Zone 1) and three of the boulders in the adjacent debris-covered Zone 2 have young exposure ages (<1.5 ka) consistent with the erratics appearing recently at the ice surface. These young exposure ages would be expected in newly accumulating fresh moraine. In contrast, the quartz-rich erratics on all ridges display scatter in exposure ages, ranging from a few thousand years to over 70,000 years. The ages of the older boulders, (13, 15, 17, 20 and 21) with exposure ages in the range 40–70 ka span much of the global Last Glacial Maximum. The available  $^{26}\text{Al}/^{10}\text{Be}$  ratios do not suggest prolonged burial of these samples. Two young  $^{10}\text{Be}$  exposure ages (19, and 22) within Zones 3 and 4 suggest that the ridges far from the exposed ice edge could still be active and bringing new material to the surface.

The  $^{36}\text{Cl}$  ages from limestone boulders are confined to Zone 2 next to the ice edge and the main ridges of Zone 3. The pattern is one of a scatter in exposure ages ranging from a few thousand years to over 50,000 years with no discernible overall trend. These boulders originated in the cliffs of a tributary glacier and could have experienced a complex history as the local ice merged with the overall ice sheet as it declined in altitude ~10,000 years ago. The source area on the cliff and the trajectory and stability of boulders once on the glacier would have changed during such lowering.

Six exposure ages on the BIM of Independence Hills are very different (Table 3). The exposure ages of two boulders on the moraine closest to the trunk glacier ice (samples IH12-21 and IH12-22) have exposure ages

of 42.6 ka and 16.6 ka, while those on a ridge composed of local lithologies further away from the glacier margin (samples IH12-19 and IH12-20) have exposure ages of 54.7 ka and 35.3 ka, while boulders in the midst of the moraine itself (samples IH12-13 and IH12-14) have young ages of 2.3 and 3.4 ka. The implication is that, as in the case of Patriot Hills moraine, the older ages show that the BIM in Independence Hills has persisted through much of the last glacial cycle, while the young ages within the moraine point to more recent continued activity (uplift, rolling of clasts etc.).

### 5. Discussion

Having described the results based upon methodological approaches it is now necessary to integrate the results to provide (i) an holistic view of BIM formation patterns in the Heritage Range; (ii) an appreciation of the link between morphology and process; (iii) the rate of BIM formation in the Heritage Range; (iv) the implications of this for other BIM, including comparison with key BIM studies elsewhere in Antarctica and; (iv) how these insight in BIM formation assist with cosmogenic studies of WAIS history.

#### 5.1. The processes that generate BIM in the Heritage Range

Fig. 12 is a conceptual model that brings together and summarises the complexity of processes forming BIM in a dynamic setting such as the Horseshoe Valley. During last glacial maxima (and likely many other previous maxima), ice in Horseshoe Valley is thicker and joined by tributaries from local valley glaciers, forming medial moraine sequences. Ice may also flow out of topographic depressions which, whilst

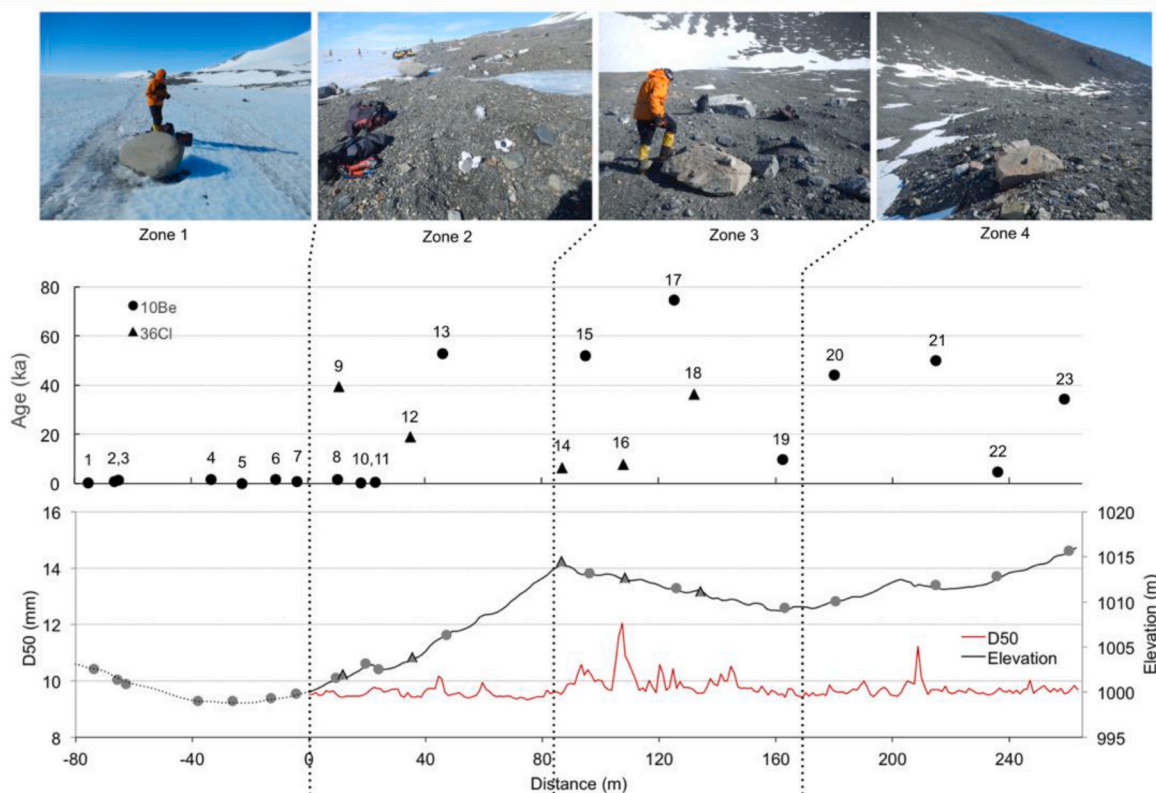


Fig. 11. A. Photographs of representative boulders in different zones that were used for cosmogenic isotope analysis. B. An age profile through Patriot Hills BIM in the main embayment showing  $^{10}\text{Be}$  (marked by circles) and  $^{36}\text{Cl}$  (marked by triangles) exposure ages plotted along the transect (PH3, Fig. 4A). C. Elevation and median grain size along the transect (with the elevations of cosmogenic nuclide samples denoted by circles and triangles). On the blue ice the clasts all show near zero age exposure, indicating they have recently ablated to the surface. Once on the moraine there is a scatter of dates ranging between a few thousand and 70,000 years. It is likely that the older boulders have been part of the moraine during much of the last glacial cycle. Fresh boulders are still brought to the surface across the width of the moraine. (For interpretation of the references to colour in this figure legend, the reader is referred to the Web version of this article.)

**Table 3**

Cosmogenic  $^{10}\text{Be}$ ,  $^{26}\text{Al}$  and  $^{36}\text{Cl}$  surface exposure ages. To calculate the surface exposure ages presented in this paper, we used default settings in Version 2.1 of the CRONUScalc programme (Marrero et al., 2016a), the CRONUS-Earth production rates (Borchers et al., 2016; Marrero et al., 2016a; Phillips et al., 2016) with the nuclide-dependent scaling of Lifton-Sato-Dunai (Lifton et al., 2014). RF denotes rockfall.

BI Zone	Sample ID	$^{10}\text{Be}$ age	$\pm 1\sigma$ (int) <sup>a</sup> $^{10}\text{Be}$	$\pm 1\sigma$ (ext) <sup>a</sup> $^{10}\text{Be}$	$^{26}\text{Al}$ age	$\pm 1\sigma$ (int) <sup>a</sup> $^{26}\text{Al}$	$\pm 1\sigma$ (ext) <sup>a</sup> $^{26}\text{Al}$	$^{26}\text{Al}/^{10}\text{Be} \pm 1\sigma$	$^{36}\text{Cl}$ age	$\pm 1\sigma$ (int) <sup>a</sup> $^{36}\text{Cl}$	$\pm 1\sigma$ (ext) <sup>a</sup> $^{36}\text{Cl}$
		(ka)	(ka)	(ka)	(ka)	(ka)	(ka)		(ka)	(ka)	(ka)
<b>Marble Hills</b>											
1	MH12-45 <sup>1</sup>	0.85	0.14	0.18	0.603	0.046	0.091	5.08 ± 1.24			
1	MH12-47 <sup>1</sup>	0.02	0.17	0.17	0.161	0.062	0.065	62.11 ± 506.94			
1	MH12-42 <sup>1</sup>	0.54	0.20	0.21							
2	MH12-55 <sup>3</sup>	28.2	1.0	3.4	26.2	1.3	3.8	6.68 ± 0.41			
<b>Independence Hills</b>											
4	IH12-13	2.30	0.32	0.44							
4	IH12-14	3.40	0.20	0.47	3.66	0.27	0.60	7.76 ± 0.72			
2	IH12-21 <sup>2</sup>	42.6	1.5	5.1	48.8	2.0	7.0	8.18 ± 0.43			
2	IH12-22 <sup>2</sup>	16.6	0.6	2.0							
3	IH12-19 <sup>2</sup>								54.7	2.3	6.7
3	IH12-20 <sup>2</sup>								35.3	1.8	4.3
RF	IH12-24								14.4	0.8	1.8
RF	IH12-25								11.2	0.6	1.3
RF	IH12-27								172	12	26
RF	IH12-29								15.0	0.9	1.9
<b>Patriot Hills</b>											
1	PH12-97 <sup>1</sup>	0.089	0.16	0.16							
1	PH12-133 <sup>1</sup>	0.82	0.17	0.20							
1	PH12-96 <sup>1</sup>	1.28	0.26	0.31	0.89	0.14	0.20	5.03 ± 1.04			
1	PH12-145 <sup>1</sup>	1.46	0.24	0.29	1.42	0.17	0.24	7.04 ± 1.29			
1	PH12-160	0.0084	0.23	0.23							
1	PH12-102	1.48	0.25	0.32	2.11	0.26	0.35	10.16 ± 1.66			
1	PH12-169	0.821	0.10	0.15							
2	PH12-165				1.51	0.27	0.32				
2	PH12-77								39.9	2.2	5.0
2	PH12-164	0.23	0.12	0.13							
2	PH12-170	0.44	0.11	0.12	0.096	0.17	0.17	1.33 ± 1.99			
2	PH12-74								19.1	1.0	2.3
2	PH12-105	52.7	1.7	6.3	55.6	2.8	8.0	7.40 ± 0.44			
3	PH12-158								6.4	0.3	0.7
3	PH12-106	51.9	2.5	6.5	52.1	3.3	7.8	7.17 ± 0.57			
3	PH12-76								7.8	1.3	1.6
3	PH12-156	74.6	2.4	8.9							
3	PH12-155								36.1	1.6	4.3
3	PH12-157	9.8	0.4	1.2							
4	PH12-152	44.1	1.3	5.2	47.3	2.0	6.7	7.68 ± 0.39			
4	PH12-148	50.0	1.6	5.9							
4	PH12-146	4.78	0.18	0.58							
4	PH12-153	34.4	1.2	4.1							
RF	PH12-79								13.4	1.4	1.7
RF	PH12-80								51.6	5.1	6.4
RF	PH12-82								9.8	1.0	1.3
RF	PH12-83								42.3	4.2	5.2

<sup>a</sup> (int) = internal uncertainty from AMS; (ext) = propagated external uncertainties including internal uncertainties plus those from scaling, production rates of cosmogenic nuclides, conservative uncertainties on thickness (0.5 cm), pressure (10 hPa), and composition (for  $^{36}\text{Cl}$  only). Data previously reported by 1Hein et al. (2016a), 2Hein et al. (2016b), and 3Sugden et al. (2017). BI Zone RF indicates rockfall.

they do not reach the ice sheet surface cross the upper trim line and redistribute clasts. The main Horseshoe Valley flow transports exotic sediments towards Patriot Hills, where clasts are transported as lateral and medial moraines or exhumed at the glacial surface by katabatic winds. At the glacial margin, these exotic clasts exist alongside local clasts, the latter predominantly derived from local ice, often derived from small-scale mass movement processes in the tributary valleys. During interglacial conditions, local valley glaciers become smaller, debris covered and no longer feed onto the ice sheet. Smaller topographically constrained glaciers retreat, stagnate and can disappear or retreat to a local snow/ice pack, leaving evidence only of cross-cut moraines.

The conceptual model further suggests that sediment concentrations

vary with distance from the glacial margin. In Zone 1, furthest from the mountain range, folded internal layers bring isolated, exotic boulders to the surface. Closer to the mountain front, in Zone 2, thin sediment layers are exhumed and concentrated by katabatic wind sublimation of the ice surface. These zones would still exist under glacial maxima conditions provided nunataks were still present (which has been the case through the Quaternary). In Zone 3 exotic and local sediments are built up in elongate ridges derived from local hanging valley medial moraines, whilst Zone 4 represents a more subdued landscape at the back of the basin, where local sediments, derived from periglacial mass movement of old till surfaces and local rockfall are mixed in with long exposed exotic clasts.

We suggest that BIM in the Heritage Range are continuously

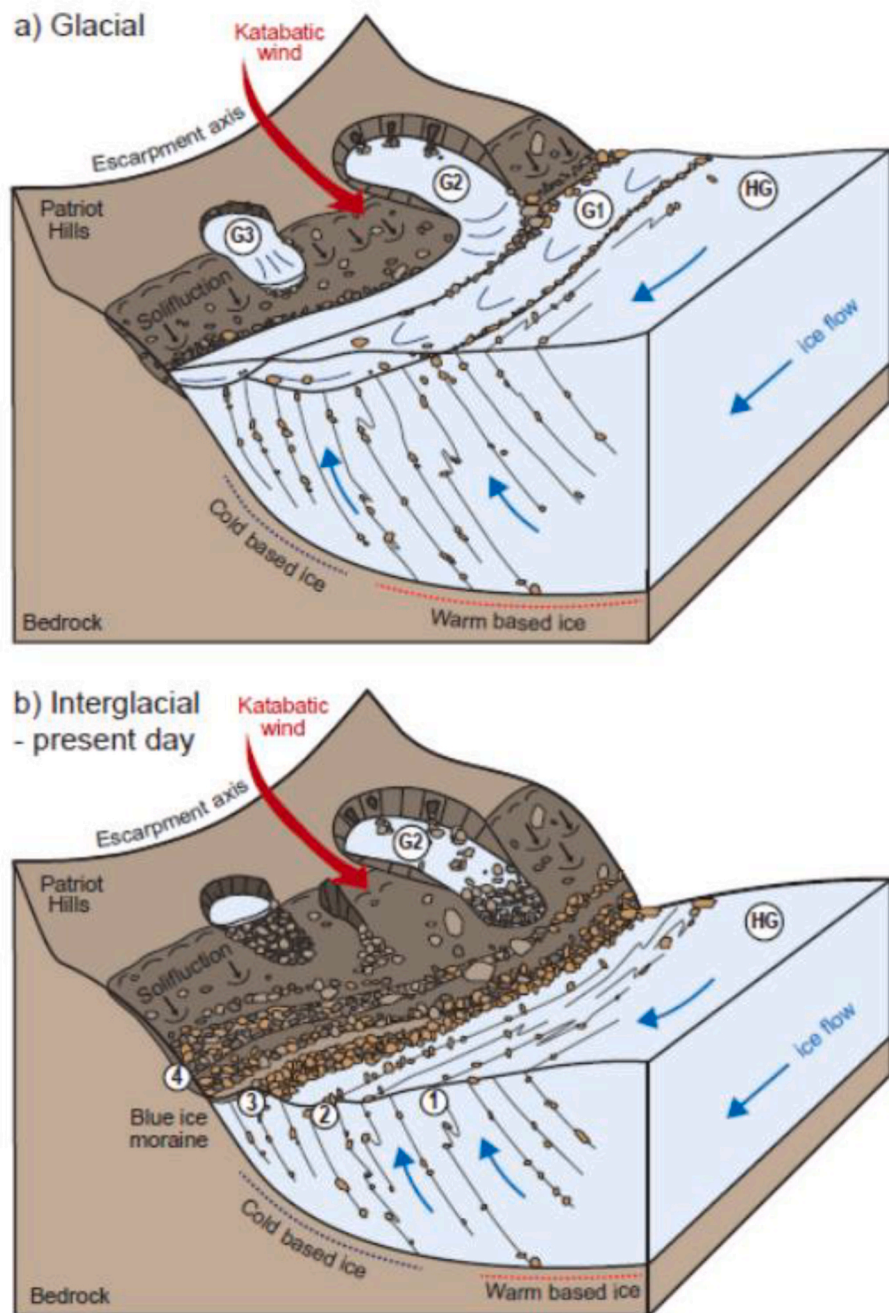


**Fig. 12.** Conceptual diagram illustrating the processes building the BIM in the Heritage Range, Antarctica during glacial maxima (a) and interglacial conditions (b). During glacial maxima Horseshoe Glacier (HG) is joined by tributary flows from local valley glaciers (G1-G2). Ice also flows out of topographic depressions, such as G3, which do not reach the ice sheet surface today but cross the upper trim line. The main regional glacial units HG and G1 transport exotic sediments towards Patriot Hills, where clasts are transported as lateral and medial moraines or exhumed at the glacial surface by katabatic winds, forming a sequence of moraine ridges of different and distinctive lithologies. At the glacial margin, these exotic clasts exist alongside local clasts, the latter predominantly derived from small-scale mass movement processes. During interglacial conditions, like today, local valley glaciers (G2) become stagnant, debris covered and no longer feed onto the ice sheet. Smaller topographically constrained glaciers retreat, stagnate and can disappear or retreat to a local snow/ice pack, leaving evidence of cross cut moraines. Sediment concentrations vary with distance from the glacial margin: in Zone 1 folded internal layers bring isolated, exotic boulders to the surface, but closer to the glacier margin (Zone 2) thin sediment layers are exhumed by katabatic wind sublimation of the ice surface. In Zone 3 mounds of exotic and local sediments are built up in elongate ridges, whilst Zone 4 represents a more subdued landscape at the back of the basin, where local sediments, derived from mass movement processes like rockfalls are mixed in with exotic clasts.

replenished with sediment from a diverse range of sedimentological sources. Much of the sediment in BIM has been derived from the glacier base. This is demonstrated by the nature of the material (lithology, roundness and surface features, striations), the occurrence of point reflectors in GPR transects, the young exposure ages of boulders on the ice surface and the pattern of debris on the glacier surface. Boulders on the ice surface are commonly associated with debris bands of finer material which can be traced on the surface as intensely folded structures (Fig. 2A). There is also evidence of boudinage (Fig. 9B). GPR shows that similar boulders and boudinage concentrations also occur further down the ice column, where they may also be associated with finer debris bands. This finding is consistent with airborne radar surveys of the ice flow between Patriot and Independence Hills, where sediment reflectors have been traced for over 1000 m, from the glacial bed to the surface of Independence Hills BIM (Hein et al., 2016a). At the surface, cosmogenic

exposure ages are young, reflecting recent exposure) from 0 to 1.5 ka. Our local airborne radar surveys suggest that subglacial debris is entrained at the transition from warm to cold-based ice (Winter et al., 2019). This is consistent with the presence of subglacial lakes in neighbouring valleys – specifically subglacial Lake Ellsworth (Ross et al., 2011), Subglacial Lake CECs (Rivera et al., 2015) and radar-derived evidence of cold-based basal ice units on neighbouring high elevation topography (Winter et al., 2015). It is assumed that sediment is entrained by freezing-on processes at the ice/bed interface as the ice passes upslope from a warm-based to a cold-based regime (Winter et al., 2019). Subsequently, the basal debris layer becomes increasingly folded and disturbed as it rises to the blue-ice ablation zone at the surface. It is this tight folding that outcrops on the ice surface (Fig. 12). The lithology of the clasts suggests that some material is derived from far afield while other material is of local origin. The quartzites and

basic igneous lithologies recorded in the moraine sequences at Patriot and Independence Hills match bedrock outcrops in the Scholt Hills some 70 km to the NNW (Denton et al., 1992). These exotic erratics represent overall flow to the SSE towards Institute Ice Stream, a direction of flow conformable with erosional landforms in the troughs and mountains in the area, and numerical modelling investigations (Hein et al., 2016a; Winter et al., 2016; Sugden et al., 2017). Some of the ridges along Independence Hills BIM comprise of a single rock type of local origin, namely a limestone, sandstone or slate, where some clasts exhibit a degree of roundness or striation, indicative of basal debris. Following a recent study of BIM in the Transantarctic Mountains by Bader et al. (2017), we suggest these single lithologies reflect a zone of freezing-on at a particular depth as the ice flows upwards towards the surface. Without more knowledge of the subglacial geology, it is impossible to know at what depth entrainment is taking place and how thick the ice was at the time of entrainment. However, the clarity of the lithological distinction and the lack of mixing with other lithologies does suggest that entrainment has been localised. One can suggest that a sequence of moraine ridges, each with a distinctive lithology, reflects a changing locus of freezing-on, perhaps related to changing ice thickness during a phase of thinning. We show these lithologically distinct ridges with the use of different coloured boulders in Fig. 12.

Fig. 12 also shows that many BIM in Patriot and Independence Hills also contain debris contributed by local ice masses. Such glaciers accumulate as wind-drift glaciers in the lee of the mountain crests lying athwart the katabatic winds. The best example is the debris-covered glacier in the middle of Patriot Hills, where buried ice extends to the foot of the mountain and merges with Horseshoe Glacier (Fig. 7B). The distinctive boulder train of limestone blocks overlies the buried ice as it swings round to align with the highest and most continuous moraine ridge extending for 3 km across the embayment to the northeast (Fig. 7B). An adjacent debris-covered glacier, mapped in Sugden et al. (2017), is pockmarked with kettle holes. It extends just far enough to truncate the main BIM and cover exotic rocks with local limestone. In Independence Hills, the arcuate structures identified in the GPR surveys and the lack of exotic clasts tell of tributary glaciers flowing from the main mountain crest. In the Patriot Hills case study, the main concentration of exotic clasts is in the long ridge closest to the main glacier and distant from local influences. The complexity of the relationships shows how the lithological make up of a BIM varies according to the topographic and glaciological context.

In the Patriot Hills case study periglacial slope processes in the form of creeping debris-mantled slopes were identified by Vieira et al. (2012) and Fogwill et al. (2012). This study has shown these lobes to be currently active and contributing yet another suite of debris to the BIM. Another example of periglacial accumulation is rockfall from a cliff with a runout distance of several hundred metres carrying large boulders onto the moraine surface (Fig. 7A). The presence of other clusters of such large, angular and broken boulders on the BIM of Independence Hills with  $^{36}\text{Cl}$  dates between 0.17 and 15 ka<sup>-1</sup> points to an intermittent process of rockfall.

A process of sediment transport that has probably been underestimated in the past is debris transport by the flow of buried ice. The most impressive example in our study site is the lobate till sheet in Marble Hills, underlain by relict glacier ice, flowing down the topographic slope (Fig. 7C and D). But there are many other examples in Patriot Hills where lobate structures indicate downslope flow towards and onto the BIM at the mountain foot. Indeed, much of the back slope of the BIM at the mountain foot may consist of slope debris transported by such flow. One interesting example occurs in Patriot Hills where a debris-covered glacier has cut a gap through an elevated moraine containing sandstone clasts and deposited them on the BIM some 200 m lower. Here three sandstone boulders have anomalously old  $^{10}\text{Be}$  exposure ages for their location of 31–44 ka (Bentley et al., 2010). The significance of such observations is that movement and the pre-exposure of surface clasts continues long after the initial stage of deglaciation.

Indeed, further complexity could also be introduced through the movement of clasts by buried ice resulting in sorting and/or turning of clasts producing younger ages.

Finally, one can also attribute some of the BIM sediments to the accumulation of tephra, windblown dust and meteorites as possible components of the BIM. In the case of Patriot Hills there is a tephra exposed on the glacier surface as a dirt zone running parallel to the BIM but on the glacier side (Fig. 2A). The katabatic winds are also strong enough to transport dust. There is no record of micrometeorites in the area yet, but there seems no reason why they should not exist.

## 5.2. The link between morphology and process

Zone 1 comprising the ice surface adjacent to the margin is a source of debris aligned in bands or as isolated boulders. The pattern of surface debris is consistent with exposure of the basal layers of the glacier due to ablation with the most extensive zones of surface debris associated with gentle surface slopes. Whereas the debris bands and their complex pattern of surface exposure can be attributed to the entrainment and subsequent folding of basal sediments as they are transferred to the surface by ablation of the blue ice surface, causing upward advection of ice and sediment the outcrop of individual boulders isolated from any debris band is less easy to explain. Isolated boulders commonly occur on the glacier side of any debris bands. Perhaps this characteristic is the result of differential sorting during the process of folding, or the exotic clasts are not basal clasts, having been transported by regional and then blue-ice flow.

Zone 2 is the zone closest to the exposed glacier ice and it slopes towards the main glacier. In common with the ice surface itself, it has the highest concentration of exotic erratics. This is the zone with most evidence of ablation and summer melting. The concentration of kettle holes, often with ice exposed, solifluction sheets 5–10 cm thick overlying glacier ice, the occurrence in summer of meltwater pools or films of water, and the existence of large boulders resting on pedestals of ice all tell of surface ablation. This ablation seemed much more common than that observed by Carrasco et al. (2000) who found ablation only during ENSO related warm periods though in a later paper Carrasco identified 47 warm periods at Patriot Hills since 1997 (Carrasco, 2018). In some locations the surface is broken up by boulders with their base fixed in the ice. Morphologically, Zone 2 seems to be evolving most rapidly.

Zone 3 is dominated by ridges that form the highest parts of the BIM at Patriot Hills. In the embayment study area, the highest ridge is dominated by locally derived limestone blocks with a scatter of exotic erratics. The ridges are marked by transverse grooves in the surface material, most of which represent splaying crevasses as the ice encroaches on the embayment. Excavation reveals boudinage with basal debris contained in the ice that, following ablation, supplies debris to the ridge (Fig. 9B). The ridges are parallel to the flow of the main trunk glacier, to the orientation of debris bands exposed on the ice, and to the mountain front. GPR suggests that each ridge represents the outcrop of a series of continuous or disrupted debris bands. This association is also clear in the case of the 4 km long Independence Hills BIM.

Zone 4 lies closest to the mountain front. Generally, the morphology is more subdued and lower than the ridges of Zone 3 and the material is finer. A splaying set of grooves in the surface material are at right angles to the curve of the embayment (Fig. 4B). We suggest these too represent the flow of active ice as it moves into the embayment. Exotic erratics are present, especially associated with ridges, but most other debris is of local lithology. Towards the mountain slope the debris is indistinguishable from that on the slope above. The existence of ridges with exotic erratics, the evidence of seasonal uplift, and the presence of splaying crevasses suggests this inner zone is still active but dominated by locally derived slope material.

We hypothesize that the overall morphology within the moraines is related to the differential thickness of debris on the surface. Thus, where the debris cover is sparse as in Zone 1, ablation is able to lower the ice

surface and create a depression at the ice/moraine interface. The GPS measurements and the constant elevation of the margin between seasons demonstrates that there is compensating upward flow of ice. Where the debris cover is thick, as in the case of Zone 3 and the ridges in subdued Zone 4, it provides more protection for the underlying ice from ablation, and this is demonstrated in the measurements of low elevation changes of  $<0.10 \text{ m a}^{-1}$  during a summer season. It is notable that the clast orientation measurements show clasts oriented downslope on the flanks of ridges and aligned parallel to depressions between ridges, both features to be expected from solifluction accompanying ablation. Thicker debris occurs where there is a concentration of entrained debris bands or boudinage or where there is an additional input from a local source. It is surely noteworthy that the highest ridge in Patriot Hills embayment is where there is evidence both of boudinage bringing basal material to the surface and an abundant supply of limestone blocks from a contributing local glacier. Zone 2 adjacent to the ice is the most dynamic zone in which ablation, coupled with upward and landward ice flow, is concentrating surface debris. The density of melt basins and abundant evidence of thin solifluction sheets (thinner than sediment depth in Zone 3 and 4) over gently sloping ice surfaces are all testament to the potential of such activity to concentrate debris.

It is interesting to consider how the morphology and extent of the zones are likely to evolve during the course of a glacial cycle. During a phase of ice sheet thinning there will be changes related both to the evolving katabatic winds and the debris supply as more and more of the nunatak topography is exposed. The dominant control on Zones 1 and 2 is the strength of the katabatic winds and this will change. As the ice thins the enhanced amplitude of the newly emerging topography will strengthen the winds and increasingly funnel them through low points in the topography. The sediment sources and thicknesses are also likely to change during a phase of ice sheet thinning. At the first stage of blue-ice formation any sediment is likely to be derived mainly from the ice-sheet base as in Zones 1 and 2. As the area and relief of the nunatak increases, local glaciers and periglacial processes will increasingly contribute sediment and add to debris thicknesses as, for example, in Zones 3 and 4.

### 5.3. The rate of BIM formation

Taking a longer-term view, the geomorphology and cosmogenic nuclide analysis shows that BIM have existed in the southernmost Ellsworth Mountains for at least 1.4 Ma and probably more than 3.5 Ma (Hein et al., 2016a; Sugden et al., 2017). During the Last Glacial Maximum, the ice sheet in the area was some 270–480 m thicker than present. The ice sheet sustained its greater thickness until around 9000–10,000 years ago when it began to thin slowly. Then 6000 years ago, it thinned suddenly to near its present level which was achieved around 3500 years ago (Hein et al., 2016b). The result of this last stage of deglaciation is seen by the preservation of relict, elevated BIM comprised of unweathered rock debris, sometimes underlain by remnants of glacier ice. There are two implications of this history. First, an understanding of the BIM of today involves understanding the effect of the last glacial cycle. Second, the current BIM may have been forming at or close to their present location and elevation for some 3500 years.

The scatter of cosmogenic nuclide ages on boulders on the BIM spans the Last Glacial Maximum and dates range from a few thousand years to over 70 ka. It also applies to ridges with exotic erratics and the boulder train of limestone boulders feeding into the BIM at the mountain front of Patriot Hills. Cosmogenic nuclide inheritance could introduce such scatter, but we argue inheritance is minimal given rocks emerging from active blue-ice are young, and where tested  $^{26}\text{Al}/^{10}\text{Be}$  ratios do not indicated prolonged burial/recycling of clasts. Measuring in-situ  $^{14}\text{C}$  may help to confirm this interpretation (e.g., Nichols et al., 2019; Akçar et al., 2020). Excluding the possible effect of inheritance, the implication is that boulders can survive on the moraine surface for tens of thousands of years during which they are mixed with younger debris. Thus, we envisage the BIM moving up and down the mountain front as the ice

thickness waxes and wanes during a glacial cycle in response to changes in ice thickness which could be orbitally induced and/or linked to the interaction of accumulation rates and ice dynamics related to ice sheet/ocean interactions at the grounding line (e.g., Ackert et al., 2011, 2013).

With respect to the age of the youngest moraine, current measurements of the rate of ablation in the seasons 2013–2014 reveal that the ice surface in Zone 1 lost 10–25 cm of ice. If such a rate is extrapolated back in time, then it would be possible for basal ice at a depth of 800 m to have appeared at the surface along with glacially entrained rock debris in 3200–8000 years. These estimates are based on simple assumptions, but the lower estimate serves to show that there is time for the current BIM to have formed since the ice sheet stabilised at the present level 3600 years ago and to have achieved dynamic equilibrium, although a much longer time period for formation is also compatible with the evidence. The young exposure ages of boulders emerging at the ice surface with ages measured in hundreds of years is clear evidence of their current activity.

There is an apparent jump in the timing of sediment emergence in the middle of Zone 2. In Zone 1 and 2 most clasts are younger than 10 ka. From the middle of Zone 2 to Zone 4, ages are a mix of  $<10$  ka and from 35 to 55 ka. Perhaps the break marks a phase of instability when the ice-sheet surface elevation was declining relatively rapidly. Detailed GPR surveys of the blue ice at Patriot Hills by Winter et al. (2016) shows discontinuities in the internal reflections, possibly suggesting a change in erosion, accumulation or regional flow of ice in the Horseshoe Valley. Work on a horizontal ice core extracted from the blue ice at Patriot Hills by Fogwill et al. (2012) indicates the discontinuities occurred around 25 ka and 10 ka. Hein et al. (2016a) interpret the latest fall in ice elevation fall to have occurred from 6.5 ka to 3.5 ka. The clustering of dates for the BIM at this site from 35 ka – 55 ka and again from 10 ka to the present day, may reflect periods of relative stability of ice-sheet flow which permitted clasts to accumulate in all four zones on the mountain front.

### 5.4. Implications for other BIM

Prevailing theories on BIM formation, presented by Akçar et al. (2020) and Kassab et al. (2020) suggest a lateral accretion model for dynamically stable moraine surfaces in East Antarctica where: (i) it is material released from surface ablation that, once concentrated, forms blue-ice moraines (BIM), (ii) that the moraine formation can be dated using cosmogenic isotope approaches, and that, (iii) since we expect an increase in exposure age moving away from the ice margin towards bedrock, dating across the moraine can be used to constrain ice-sheet history. We also observe fine dipping reflectors within the ice on GPR profiles, as seen at Mount Acheron in East Antarctica. This indicates that lateral accretion is a ubiquitous process across many East and West Antarctic BIM.

In contrast to observations at Mount Acheron we find that once sediment coalesces in BIM through lateral accretion, significant reworking occurs through differential ablation, slope and periglacial processes. These observations have allowed the further development of the model proposed for the Patriot Hills BIM by Fogwill et al. (2012). In particular, the influence of local glaciers overriding or merging with the main ice stream surface, as also suggested from englacial reflectors by Campbell et al. (2013) in the Pensacola Mountains, provides a further mechanism for clasts of different exposure ages to be deposited onto the BIM surface. We bring these processes together with lateral accretion in our conceptual model. The model suggests that many BIM in West Antarctica are dynamic and, whilst they persist through glacial cycles, they do not always neatly record ice sheet retreat patterns since linear distance from the ice margin does not always relate to increased clast exposure age.

### 5.5. Do these insights assist with cosmogenic studies of WAIS decay?

The different sources of debris and changing ice dynamics shown in Fig. 12 help to explain why moraines in Antarctica have often produced a scatter of exposure ages. It has been common to assume that the youngest ages must represent the time of effective deposition by a thinning glacier (Bentley et al., 2010; Hein et al., 2016b; Stone et al., 2003). However, BIM are prone to buried-ice features which could cause samples to appear too young rather than too old (Todd et al., 2010). In view of the evidence of exposure by surface ablation and disturbances associated with subsequent flow beneath a debris cover, the commonly used 'youngest age' assumption may in this situation underestimate the age of thinning since the Last Glacial Maximum. The role of buried glacial ice is in addition to other physical processes, such as erosion, cracking, and rolling, that can expose fresh surfaces or remove accumulated nuclides, yielding ages that are too young (Gosse and Phillips, 2001). In such situations the youngest ages do not represent the date of initial deglaciation but of the final loss of the buried ice. This process is most likely to be significant in BIM due to the debris accumulation on the surface.

Ice sheet elevation history may be further complicated by the fact that it is nearly impossible to determine if a moraine or drift area was previously ice-cored if no ice remains today. The potential time frame for these effects can be significant, as seen by the survival of buried ice for at least 8.1 Ma in Beacon Valley, East Antarctica (Sugden et al., 1995). The degree of displacement of samples from their position at the time of ice abandonment is also significant. Swanger et al. (2010) measured glacier-ice cored lobes of similar thickness to that measured in this study (14–30 m thick compared to 10–15 m measured in this study) moving at average speeds of 4–4.5 mm yr<sup>-1</sup>.

The implication is that a better understanding of the processes of BIM formation helps in assessing the significance of any boulder that is a target for exposure age dating, especially in terms of its emplacement and relationship to ice dynamics. We can highlight the following observations based on our experience: (a) In using a blue-ice deposit to study deglaciation, the clearest results come from analysis of clasts known to have been derived from the glacier base, a conclusion also reached by Akçar et al. (2020). In our study of deglaciation, we targeted striated clasts wherever possible (Hein et al., 2016a, 2016b). (b) The presence of locally derived debris can contribute boulders with inheritance, more so than sub-glacially derived exotic debris. Such a situation occurs in the case of the debris-covered glacier in Patriot Hills; here cliff collapse can involve rock faces with prior exposure. The inverse problem can apply to recognition of rockfall debris; here the cosmogenic ages may date an event much younger than the moraine, as in the case of the rockfall in Independence Hills. (c) The identification of the possible impact of buried glacier ice is important. Buried ice flows down the local topographic slope and as it decays fresh boulders are brought to the surface. One would expect both an increased scatter of ages and also a series of dates that are younger than the date the ice sheet abandoned a site. (d) All the ridges in a suite of BIM in an area may be active. Our initial interpretation of Zone 4 was that it was an older, more subdued surface, but the observation that during one-month boulders were moving throughout the BIA revealed a more dynamic picture. This was reinforced by rare young exposure ages discovered in ridges far from the ice margin. Such dates have little bearing on the age of the moraine but demonstrate the activity of the whole. (e) We found it helpful to study key sites such as bedrock spurs, to avoid possible zones of dead ice, and (f) to measure multiple closely located clasts using multiple cosmogenic nuclides to check scatter at crucial sites. In-situ <sup>14</sup>C may prove valuable for testing inheritance and for constraining the late glacial and Holocene ice history.

## 6. Conclusion

BIM in the southernmost Ellsworth Mountains are equilibrium forms

reflecting a balance between sediment supply by ice and debris flowing upwards into localised ablation areas in the lee of mountain ridges. Cosmogenic nuclide analysis shows that boulders may survive in a BIM during the course of glacial cycles. During such a cycle the moraine moves up and down the mountain front in response to the changing thickness of the ice sheet.

This study shows that the bulk of the debris in the BIM is eroded from deep within the glacier and rises to the surface over thousands of years. At the surface it is mixed with debris supplied by local glaciers and slope processes. Following a period of ice sheet thinning, remnants of BIM may continue to flow and/or ablate and disturb surface debris for thousands of years. Understanding the interaction between different origins of sediment and between ice sheet and local glaciers helps target the optimum boulders to sample for surface exposure age dating.

Early readers of this paper have commented that the problems of using BIM in West Antarctica are so complex that one understandable reaction is never to use them for establishing ice-sheet history! Our response is to say that once the topographic and glaciological relationships become clearer, evidence from BIM opens a window into Antarctic ice-sheet history extending back several million years. Moreover, the presence, absence or persistence of a BIM at a particular time provides information on past ice-sheet behaviour, as we have shown in the Heritage Range (Hein et al., 2016a, 2016b). In an ice-sheet location such as Horseshoe Valley where ice-sheet thickness varies markedly during a glacial cycle, BIM can only form when a mountain has emerged from beneath a thinning ice-sheet surface. Thus, there will be periods with no BIM formation. Further, the balance between local and exotic clasts will change as the elevation changes. In locations such as the higher summits of the Transantarctic Mountains analysis of BIM points to a longer and more stable history (Bader et al., 2017; Balco et al., 2014).

Another scientific opportunity arises from the presence of basal ice and debris at the ice-sheet surface. This provides easy access to basal ice and, as has been shown in the Transantarctic Mountains, analysis can tell of the basal processes that influence the dynamics of the wider Antarctic Ice Sheet.

## Declaration of competing interest

The authors declare that they have no known competing financial interests or personal relationships that could have appeared to influence the work reported in this paper.

## Acknowledgements

The research was funded by the UK Natural Environment Research Council grant numbers NE/I025840/1, NE/I027576/1, NE/I024194/1 and NE/I025263/1. We thank the British Antarctic Survey for logistical support and Scott Webster, Malcolm Airey and Phil Stevens for field support. Reed Scherer kindly checked till samples for marine diatoms.

## References

- Ackert, R.P., Mukhopadhyay, S., Parized, B.R., Borns, H.W., 2007. Ice elevation near the West Antarctic ice sheet divide during the last glacial maximum and its subsequent retreat history: a review. *Geophys. Res. Lett.* 34, L21506.
- Ackert, R.P., Mukhopadhyay, S., Pollard, D., DeConto, R.M., Putnam, A.E., Borns, H.W., 2011. West Antarctic Ice Sheet elevations in the Ohio Range: geologic constraints and ice sheet modeling prior to the last highstand. *Earth Planet Sci. Lett.* 307, 83–93.
- Ackert, R.P., Putnam, A.E., Mukhopadhyay, S., Pollard, D., DeConto, R.M., Kurz, M.D., Borns, H.W., 2013. Controls on interior West Antarctic Ice Sheet Elevations: inferences from geologic constraints and ice sheet modelling. *Quat. Sci. Rev.* 65, 26–38.
- Akçar, N., Yesilyurt, S., Hippe, K., Christl, M., Vockenhuber, C., Yavuz, V., Özsoy, B., 2020. Build-up and chronology of blue ice moraines in Queen Maud Land, Antarctica. *Quat. Sci. Adv.* 2, 1–12.
- Altmair, M., Hergers, U., Delisle, G., Merchel, S., Ott, U., 2010. Glaciation history of Queen Maud Land (Antarctica) reconstructed from in-situ produced cosmogenic <sup>10</sup>Be, <sup>26</sup>Al and <sup>21</sup>Ne. *Pol. Sci.* 4, 42–61.

- Bader, N.A., Licht, K.J., Kaplan, M.R., Kassab, C., Winckler, G., 2017. East Antarctic ice sheet stability recorded in a high-elevation ice-cored moraine. *Quat. Sci. Rev.* 159, 88–102.
- Balco, G., Stone, J.O.H., Sliwinski, M.G., Todd, C., 2014. Features of the glacial history of the Transantarctic Mountains inferred from cosmogenic  $^{26}\text{Al}$ ,  $^{10}\text{Be}$  and  $^{21}\text{Ne}$  concentrations in bedrock surfaces. *Antarct. Sci.* 26, 708–723.
- Bentley, M.J., Fogwill, C.J., Le Brocq, A.M., Hubbard, A.L., Sugden, D.E., Dunai, T.J., Freeman, S.P.H.T., 2010. Deglacial history of the West Antarctic ice sheet in the Weddell Sea embayment: constraints on past ice volume change. *Geology* 38, 411–414.
- Bibby, T., Putkonen, J., Morgan, D., Balco, G., Shuster, D.L., 2016. Million year old ice found under meter thick debris layer in Antarctica. *Geophys. Res. Lett.* 43, 6995–7001.
- Bintanja, R., 1999. On the glaciological, meteorological, and climatological significance of blue ice areas. *Rev. Geophys.* 37, 337–359.
- Borchers, B., Marrero, S., Balco, G., Caffee, M., Goehring, B., Lifton, N., Nishiizumi, K., Phillips, F., Schaefer, J., Stone, J., 2016. Geological calibration of spallation production rates in the CRONUS-Earth project. *Quat. Geochronol.* 31, 188–198.
- Bradley, S.L., Hindmarsh, R.C.A., Whitehouse, P.L., Bentley, M.J., King, M.A., 2015. Low postglacial rebound rates in the Weddell Sea due to Late Holocene ice-sheet advance. *Earth Planet Sci. Lett.* 413, 79–89.
- Campbell, S., Balco, G., Todd, C., Conway, H., Huybers, K., Simmons, C., Vermeulen, M., 2013. Radar-detected englacial stratigraphy in the Pensacola Mountains, Antarctica: implications for recent changes in ice flow and accumulation. *Ann. Glaciol.* 54 (63), 91–100.
- Carrasco, J.F., 2018. Contextualizing the 1997 warm event observed at Patriot Hills in the interior of West Antarctica. *Polar Res.* 37, 1547041.
- Carrasco, J.F., Casassa, G., Rivera, A., 2000. A warm event at Patriot Hills, Antarctica: an ENSO related phenomenon?. In: Sixth International Conference on Southern Hemisphere Meteorology and Oceanography, April 3, 2000, Santiago, Chile. American Meteorological Society, Boston, MA, pp. 240–241.
- Casassa, G., Rivera, A., Lange, H., Cárdenas, C., 2000. Estudios Glaciológicos en Patriot Hills, Antártica. IX Congr. Geol. Chileno, Puerto Varas, Chile 2, 359–363.
- Casassa, G., Rivera, A., Acuna, C., Brecher, H., Lange, H., 2004. Elevation change and ice flow at Horseshoe Valley, Patriot Hills, West Antarctica. *Ann. Glaciol.* 39, 20–28.
- Chmieleff, J., von Blanckenburg, F., Kossert, K., Jakob, D., 2010. Determination of the Be-10 half-life by multicollector ICP-MS and liquid scintillation counting. *Nucl. Instrum. Methods Phys. Res. Sect. B Beam Interact. Mater. Atoms* 268, 192–199.
- Dahe, Q., Petit, J.R., Jouzel, J.R., Stievernard, M., 1994. Distribution of stable isotopes in snow along the route of the 1990 International Trans-Antarctic Expedition. *J. Glaciol.* 40, 107–118.
- De Keyser, M., 2004. In: Turner, J., Pendlebury, S. (Eds.), *The International Weather Forecasting Handbook*. British Antarctic Survey, Cambridge.
- Denton, G.H., Bockheim, J.G., Rutford, R.H., Andersen, B.G., 1992. Glacial history of the Ellsworth mountains, West Antarctica. *Geol. Soc. Am. Bull.* 170, 403–432.
- Fogwill, C.J., Hein, A.S., Bentley, M.J., Sugden, D.E., 2012. Do blue-ice moraines in the heritage range show the West Antarctic ice sheet survived the last interglacial? *Palaeogeogr. Palaeoclimatol. Palaeoecol.* 335, 61–70.
- Gosse, J.C., Phillips, F.M., 2001. Terrestrial in situ cosmogenic nuclides: theory and application. *Quat. Sci. Rev.* 20, 1475–1560.
- Graly, J.A., Licht, K.J., Kassab, C.M., Bird, B.W., Kaplan, M.R., 2018. Warm-based basal sediment entrainment and far-field Pleistocene origin evidenced in central Transantarctic blue ice through stable isotopes and internal structures. *J. Glaciol.* 64, 185–196.
- Hättestrand, C., Johansen, N., 2005. Supraglacial moraines in Scharffenbergbotnen, Heimfrontfjella, Dronning Maud Land, Antarctica – significance for reconstructing former blue ice areas. *Antarct. Sci.* 17, 225–236.
- Hein, A.S., Sugden, D.E., Fogwill, C.J., Xu, 2014. Geological scatter of cosmogenic-nuclide exposure ages in the Shackleton Range, Antarctica: implications for glacial history. *Quat. Geochronol.* 19, 52–66.
- Hein, A.S., Woodward, J., Marrero, S.M., Dunning, S.A., Steig, E.J., Freeman, S.P.H.T., Stuart, F.M., Winter, K., Westoby, M.J., Sugden, D.E., 2016a. Evidence for the stability of the West Antarctic ice sheet divide for 1.4 million years. *Nat. Commun.* 7, 10325.
- Hein, A.S., Marrero, S.M., Woodward, J., Dunning, S.A., Winter, K., Westoby, M.J., Freeman, S., Shanks, R.P., Sugden, D.E., 2016b. Mid-Holocene pulse of thinning in the Weddell Sea sector of the West Antarctic ice sheet. *Nat. Commun.* 7, 12511 <https://doi.org/10.1038/ncomms12511>.
- Kaplan, M.R., Licht, K.J., Winckler, G., Schaefer, J.M., Bader, N., Mathieson, C., Roberts, M., Kassab, C.M., Schwartz, R., Graly, J.A., 2017. Middle to late Pleistocene stability of the central East Antarctic ice sheet at the head of law glacier. *Geology* 45 (11), 963–966.
- Kassab, C.M., Licht, K.J., Petersson, R., Lindbäck, K., Graly, J.A., Kaplan, M.R., 2020. Formation and evolution of an extensive blue ice moraine in central Transantarctic Mountains, Antarctica. *J. Glaciol.* 66, 49–60.
- Korschinek, G., Bergmaier, A., Faestermann, T., Gerstmann, U.C., Knie, K., Rugel, G., Wallner, A., Dillmann, I., Dollinger, G., von Gostomski, C.L., Kossert, K., Maiti, M., Poutivsev, M., Remmert, M., 2010. A new value for the half-life of Be-10 by Heavy-Ion Elastic Recoil Detection and liquid scintillation counting. *Nucl. Instrum. Methods Phys. Res. Sect. B Beam Interact. Mater. Atoms* 268, 187–191.
- Lifton, N., Sato, T., Dunai, T.J., 2014. Scaling in situ cosmogenic nuclide production rates using analytical approximations to atmospheric cosmic-ray fluxes. *Earth Planet Sci. Lett.* 386, 149–160.
- Marrero, S.M., Phillips, F.M., Borchers, B., Lifton, N., Aumer, R., Balco, G., 2016a. Cosmogenic nuclide systematics and the CRONUScal program. *Quat. Geochronol.* 31, 160–187.
- Marrero, S.M., Phillips, F.M., Caffee, M.W., Gosse, J.C., 2016b. CRONUS-Earth cosmogenic Cl-36 calibration. *Quat. Geochronol.* 31, 199–219.
- Marrero, A.M., Hein, A.S., Naylor, M., Attal, M., Shanks, R., Winter, K., Woodward, J., Dunning, S., Westoby, M., Sugden, D., 2018. Controls on subaerial erosion rates in Antarctica. *Earth Planet Sci. Lett.* 501, 56–66.
- Mills, S.C., Le Brocq, A.M., Winter, K., Smith, M., Hillier, J., Ardakova, E., Boston, C.M., Sugden, D., Woodward, J., 2019. Testing and application of a model for snow redistribution (Snow\_Blow) in the Ellsworth mountains, Antarctica. *J. Glaciol.* 65, 957–970.
- Mouginot, J., Rignot, E., Scheuchl, B., Millan, R., 2017. Comprehensive annual ice sheet velocity mapping using Landsat-8, Sentinel-1, and RADARSAT-2 data. *Rem. Sens.* 9, 364.
- Nichols, K., Goehring, B.M., Balco, G., Johnson, J.S., Hein, A.S., Todd, C., 2019. New last glacial maximum ice thickness constraints for the Weddell Sea sector, Antarctica. *Cryosphere* 13, 2935–2951.
- Nishiizumi, K., 2004. Preparation of Al-26 AMS standards. *Nucl. Instrum. Methods Phys. Res., Sect. B* 223–224, 388–392.
- Nishiizumi, K., Imamura, M., Caffee, M.W., Southon, J.R., Finkel, R.C., McAninch, J., 2007. Absolute calibration of Be-10 AMS standards. *Nucl. Instrum. Methods Phys. Res. Sect. B Beam Interact. Mater. Atoms* 258, 403–413.
- Palmer, E.F., Licht, K.J., Swope, R.J., Hemming, S.R., 2012. Nunatak moraines as a repository of what lies beneath the east Antarctic ice sheet. *Geol. Soc. Am. Spec. Pap.* 487, 97–104.
- Phillips, F.M., Argento, D.C., Balco, G., Caffee, M.W., Clem, J., Dunai, T.J., Finkel, R., Goehring, B., Gosse, J.C., Hudson, A.M., Jull, A.J.T., Kelly, M.A., Kurz, M., Lal, D., Lifton, N., Marrero, S.M., Nishiizumi, K., Reedy, R.C., Schaefer, J., Stone, J.O.H., Swanson, T., Zreda, M.G., 2016. The CRONUS-Earth Project: a synthesis. *Quat. Geochronol.* 31, 119–154.
- Rignot, E., Mouginot, J., Scheuchl, B., 2017. MEaSUREs InSAR-Based Antarctica Ice Velocity Map, Version 2, Boulder, Colorado, NASA National Snow and Ice Data Centre Distributed Active Archive Centre. <https://doi.org/10.5067/D7GK8F5J8M8R>.
- Rivera, A.R., Zamora, J., Uribe, R., Jaña, Oberreuter, J., 2014. Recent ice dynamic and surface mass balance of Union glacier in the West Antarctic ice sheet. *Cryosphere* 8, 1445–1456.
- Rivera, A., Zamora, R., Rada, C., Walton, J., Proctor, S., 2010. Glaciological investigations on Union glacier, Ellsworth mountains, West Antarctica. *Ann. Glaciol.* 51, 91–96.
- Rivera, A., Uribe, J., Zamora, R., Oberreuter, J., 2015. Subglacial Lake CECs: discovery and in situ survey of a privileged research site in West Antarctica. *Geophys. Res. Lett.* 42, 3944–3953.
- Ross, N., Siegert, M.J., Woodward, J., Smith, A.M., Corr, H.F.J., Bentley, M.J., Hindmarsh, R.C.A., King, E.C., Rivera, A., 2011. Holocene stability of the Amundsen-Weddell ice divide, West Antarctica. *Geology* 39, 935–938.
- Scherer, P., Schultz, L., Neupert, U., Knauer, M., Neumann, S., Leya, I., Michel, R., Mokos, J., Lipschutz, M.E., Metzler, K., Suter, M., Kubik, P.W., 1997. Allan Hills 88019: an Antarctic H-chondrite with a very long terrestrial age. *Meteoritics Planet Sci.* 32, 769–773.
- Schytt, V., 1961. Glaciology IIE. Blue Ice Fields, Moraine Features and Glacier Fluctuations. Norwegian-British-Swedish Antarctic Expedition, 1949–52, Scientific Results. IVE, pp. 183–204.
- Sinisaalo, A., Grinsted, A., Moore, J.C., Meijer, H.A.J., Martma, T., Van De Val, R.S.W., 2007. Inferences from stable water isotopes on the Holocene evolution of Scharffenbergbotnen blue-ice area, East Antarctica. *J. Glaciol.* 53, 427–434.
- Spaulding, N.E., Higgins, J.A., Kurbatov, A.V., Bender, M.L., Arcone, S.A., Campbell, S., Dunbar, N.W., Chmiak, L.M., Introne, D.S., Mayewski, P.A., 2013. Climate archives from 90 to 250 ka in horizontal and vertical ice cores from the Allan Hills blue ice area, Antarctica. *Quat. Sci.* 80, 562–574.
- Stone, J.O., Balco, G.A., Sugden, D.E., Caffee, M.W., Sass 3rd, L.C., Cowdery, S.G., Siddoway, C., 2003. Holocene deglaciation of Marie Byrd land, West Antarctica. *Science* 299, 99–102.
- Sugden, D.E., Marchant Jr., D.R., Potter, N., Souchez, R.A., Denton III, G.H., Wisher, C.C., Tison, J.-L., 1995. Preservation of Miocene glacier ice in East Antarctica. *Nature* 376, 412–414.
- Sugden, D.E., Hein, A.S., Woodward, J., Marrero, S.M., Rodes, A., Dunning, S.A., Stuart, F.M., Freeman, S.P.H.T., Winter, K., Westoby, M.J., 2017. The million-year evolution of the glacial trimline in the southernmost Ellsworth Mountains, Antarctica. *Earth Planet Sci. Lett.* 469, 47–52 (Corrigendum).
- Swanger, K.M., Marchant, D.R., Kowalewski, D.E., Head, J.W., 2010. Viscous flow lobes in central Taylor Valley, Antarctica: origin as remnant buried glacial ice. *Geomorphology* 120, 174–185.
- Takahashi, S., Endoh, T., Azuma, N., Meshida, S., 1992. Bare ice fields developed in the interior part of Antarctica. *Proc. NIPR Symp. Polar Meteorol. Glaciol.* 5, 128–139.
- Todd, C., Stone, J., Conway, H., Hall, B., Bromley, G., 2010. Late quaternary evolution of Reedy glacier, Antarctica. *Quat. Sci. Rev.* 29, 1328–1341.
- Turney, C.S.M., Fogwill, C.J., Gollidge, N.R., McKay, N.P., van Sebille, E., Jones, R.T., Etheridge, D., Rubino, M., Thornton, D.P., Davies, S.M., Ramsey, C.B., Thomas, Z.A., Bird, M.I., Munksgaard, N.C., Kohno, M., Woodward, J., Winter, K., Weyrich, L.S., Rootes, C.M., Millman, H., Albert, P.G., Rivera, A., van Ommen, T., Curran, M., Moy, A., Rahmstorf, S., Kawamura, K., Hillenbrand, C.D., Weber, M.E., Manning, C. J., Young, J., Cooper, A., 2020. Early Last Interglacial ocean warming drove substantial ice mass loss from Antarctica. *Proc. Natl. Acad. Sci. U.S.A.* 117 (8), 3996–4006. <https://doi.org/10.1073/pnas.1902469117>.
- Turney, C., Fogwill, C., Van Ommen, T.D., Moy, A.D., Etheridge, D., Rubino, M., Curran, M.A.J., Rivera, A., 2013. Late Pleistocene and early Holocene change in the

- Weddell Sea: a new climate record from the Patriot Hills, Ellsworth mountains, West Antarctica. *J. Quat. Sci.* 28, 697–704.
- Vieira, R., Hinata, S., Kellem da Rosa, K., Zilbertson, S., Cardia Simoes, J., 2012. Periglacial features in Patriot Hills, Ellsworth mountains, Antarctica. *Geomorphology* 155, 96–101.
- Webers, G.F., Craddock, C., Spletstoesser, J.F., 1992. Geological History of the Ellsworth Mountains, West Antarctica. *Geol. Soc. Amer. Memoir*, p. 170.
- Westoby, M.J., Dunning, S.A., Woodward, J., Hein, A.S., Marrero, S.M., Winter, K., Sugden, D.E., 2015. Sedimentological characterization of Antarctic moraines using UAVs and Structure-from-Motion photogrammetry. *J. Glaciol.* 611088–611102.
- Westoby, M.J., Dunning, S.A., Woodward, J., Hein, A.S., Marrero, S.M., Winter, K., Sugden, D.E., 2016. Interannual surface evolution of an Antarctic blue-ice moraine using multi-temporal DEMs. *Earth Sur. Dyn.* 4, 515–529.
- Whillans, I.M., Cassidy, W.A., 1983. Catch a falling star: meteorites and old ice. *Science* 222, 55–57.
- Winter, K., Woodward, J., Dunning, S.A., Turney, C.S.M., Fogwill, C.J., Hein, A.S., Gollidge, N.R., Bingham, R.G., Marrero, S.M., Sugden, D.E., Ross, N., 2016. Assessing the continuity of the blue ice climate record at Patriot Hills, Horseshoe Valley, West Antarctica. *Geophys. Res. Lett.* 43, 2019–2026.
- Winter, K., Woodward, J., Ross, N., Dunning, S.A., Hein, A.S., Westoby, M.J., Culberg, R., Marrero, S.M., Schroeder, D.M., Sugden, D.E., Siegert, M.J., 2019. Radar-detected englacial debris in the West Antarctic ice sheet. *Geophys. Res. Lett.* 46, 10454–10462.
- Wolstencroft, M., King, M.A., Whitehouse, P.L., Bentley, M.J., Nield, G.A., King, E.C., McMillan, M., Shepherd, A., Barletta, V., Bordoni, A., Riva, R.E.M., Didova, O., Gunter, B.C., 2015. Uplift rates from a new high-density GPS network in Palmer Land indicate significant late Holocene ice loss in the southwestern Weddell Sea. *Geophys. J. Int.* 203, 737–754.
- Woodward, J., Ashworth, P.J., Best, J.L., Sambrook Smith, G.H., Simpson, C.J., 2001. The use and application of GPR in sandy fluvial environments: methodological considerations. In: Bristow, C.S., Jol, H.M. (Eds.), *Ground Penetrating Radar in Sediments*, 211, vol. 211. *Geol. Soc. Sp. Pubs*, pp. 127–142.
- Xu, S., Dougans, A.B., Freeman, S., Schnabel, C., Wilcken, K.M., 2010. Improved Be-10 and Al-26-AMS with a 5 MV spectrometer. *Nucl. Instrum. Methods Phys. Res. Sect. B Beam Interact. Mater. Atoms* 268, 736–738.